David Sousa Almeida

Mapeamento Magnético para Navegação Robótica em Ambientes Interiores

Magnetic Mapping for Robot Navigation in Indoor Environments

Universidade de Aveiro
2021

David Sousa Almeida

Mapeamento Magnético para Navegação Robótica em Ambientes Interiores

Magnetic Mapping for Robot Navigation in Indoor Environments

Dissertação apresentada à Universidade de Aveiro para cumprimento dos requisitos necessários à obtenção do grau de Mestre em Engenharia Eletrónica e Telecomunicações, realizada sob a orientação científica do Doutor Francisco José Curado Mendes Teixeira, Investigador Nível 2 do Departamento de Eletrónica, Telecomunicações e Informática da Universidade de Aveiro, e do Doutor Eurico Farinha Pedrosa, Investigador Nível 1 do Departamento de Eletrónica, Telecomunicações e Informática da Universidade de Aveiro.

Dedico este trabalho aos meus pais, por todo o apoio que sempre me deram.

o júri / the jury

presidente / president

Professor Doutor António José Ribeiro Neves
Professor Auxiliar do Departamento de Eletrónica, Telecomunicações e Informática da Universidade de Aveiro

vogais / examiners committee

Doutor Alberto Manuel Martinho Vale
Investigador Auxiliar do Instituto Superior Técnico da Universidade de Lisboa

Doutor Francisco José Curado Mendes Teixeira
Investigador Nível 2 do Departamento de Eletrónica, Telecomunicações e Informática da Universidade de Aveiro

agradecimentos / acknowledgements

Desde o início do meu percurso académico que contei com a confiança e o apoio de inúmeras pessoas e instituições, sem as quais a realização desta dissertação não teria sido possível. Gostaria de expressar o meu reconhecimento para com as pessoas que contribuíram para o meu crescimento pessoal e profissional. Em primeiro lugar, quero prestar o meu agradecimento aos meus orientadores, Doutor Francisco Curado e Doutor Eurico Pedrosa, pela excelente orientação; por todo o conhecimento que me transmitiram em todos os projetos que me deram a oportunidade de participar; por toda a dedicação, compreensão e amizade manifestadas; pelos desafios cada vez mais complexos que me colocaram e pelo estímulo e exigência crescentes. Obrigado por todo o vosso apoio e por tornarem o meu percurso académico bastante mais enriquecido. Quero também agradecer à Universidade de Aveiro pelos recursos e meios disponibilizados, sem os quais a realização desta dissertação não teria sido possível. Finalmente, agradeço à minha família e amigos, em particular aos meus pais, que sempre acreditaram em mim e me deram força para seguir em frente e superar todas as adversidades que foram surgindo pelo caminho.

Palavras Chave

Navegação robótica, localização em espaços interiores, mapeamento magnético, filtro de partículas.

Resumo

A localização sempre fui um dos problemas fundamentais a resolver no âmbito da navegação robótica. O surgimento do GPS veio a servir de solução para bastantes sistemas de localização em ambientes exteriores. No entanto, a exatidão do GPS nem sempre é suficiente e os sistemas baseados em GPS falham frequentemente e não são aplicáveis em ambientes interiores. À vista disso, hoje existe uma variedade de tecnologias de localização em tempo real. É bastante comum verificarem-se anomalias magnéticas em ambientes interiores, que provêm de objetos ferromagnéticos, como infraestruturas de betão ou aço. Na navegação robótica baseada na leitura do campo magnético convencional, que utiliza a direção do campo magnético terrestre para determinar a orientação, estas anomalias são vistas como indesejáveis. No entanto, se o ambiente for rico em anomalias com variabilidade local suficiente, estas podem ser mapeadas e utilizadas como características para efeitos de localização. O trabalho apresentado nesta dissertação visa a demonstrar que é possível conjugar as medidas odométricas de um robô móvel com medições do campo magnético, para efetivamente localizar o robô em tempo real num ambiente interior. Para esse efeito, é necessário mapear o espaço de navegação e desenvolver um algoritmo de localização. Primeiramente, são apresentadas as questões abordadas para criar um mapa magnético, nomeadamente as aquisições de dados, os métodos de interpolação e os processos de validação. Posteriormente, é retratado o algoritmo de localização desenvolvido, baseado num filtro de partículas, assim como os respetivos testes experimentais de validação.

Keywords

Robot navigation, localization in indoor environments, magnetic mapping, particle filter.

Abstract

Localization has always been one of the fundamental problems in the field of robotic navigation. The emergence of GPS came as a solution for localization systems in outdoor environments. However, the accuracy of GPS is not always sufficient and GPS based systems often fail and are not suited for indoor environments. Considering this, today there is a variety of real time localization technologies. It is quite common to see magnetic anomalies in indoor environments, which arise due to the presence of ferromagnetic objects, such as concrete or steel infrastructures. In the conventional ambient magnetic field based robotic navigation, which uses the direction of the Earth's magnetic field to determine orientation, these anomalies are seen as undesirable. However, if the environment is rich in anomalies with sufficient local variability, they can be mapped and used as features for localization purposes. The work presented in this dissertation aims at demonstrating that it is possible to combine the odometric measurements of a mobile robot with magnetic field measurements, in order to effectively estimate the position of the robot in real time in an indoor environment. For this purpose, it is necessary to map the navigation space and develop a localization algorithm. First, the issues addressed to create a magnetic map are presented, namely data acquisition, employed interpolation methods and validation processes. Subsequently, the developed localization algorithm, based on a particle filter, is depicted, as well as the respective experimental validation tests.

Contents

List of Figures

List of Tables

CHAPTER 1

Introduction

Navigation is a central subject of mobile robotics and refers to how an agent finds its way in an environment. The subject of navigation can be divided into various topics. Two of these topics are mapping and localization. The first refers to how the map is generated from the robot's sensors, effectively attributing quantities and parameters to spatial regions or points in the environment. The second refers to how the robot uses the map of the environment and its sensors to finds its pose in that same environment.

Some of the more conventional robotic navigation systems measure the Earth's magnetic field to determine an orientation. The work presented in this dissertation aims at taking advantage of the distortion of the Earth's magnetic field, prevalent in many indoor environments, to determine the position of a mobile robot. For this purpose, the magnetic field of an indoor environment is mapped. Subsequently, a localization algorithm, based on a particle filter, is developed, which uses the magnetic map and magnetic field measurements to correctly estimate the robot's trajectory.

1.1 Motivation

Many indoor environments present diverse magnetic anomalies, due to the distortion of the Earth's magnetic field by ferromagnetic objects, such as steel and reinforced concrete structures. The intensity of these magnetic anomalies is usually high enough to be detected by a standard magnetometer. If the magnetic map presents a rich diversity of magnetic anomalies, static in time and spread through space with enough local variability, these can be used as features for localization and navigation purposes.

The emergence of GPS came as a solution for many of real time localization systems in outdoor environments. However, for most indoor environments, GPS has been shown to be an unreliable and unsuitable localization method. The more popular alternatives to GPS require the installation of fixed beacons, as well as line-of-sight between them. There are some alternatives that do not require the installation of fixed position sensors, such as LIDAR or vision based systems, but these are usually expensive or complex.

The solution presented in this dissertation, does require a ground truth system to create a magnetic map of the environment. Nevertheless, after the mapping phase, the developed localization algorithm only requires the magnetic field measurements acquired by a magnetometer and the wheel odometry data of the robot. Another advantage, when compared with other common indoor localization methods, is the price and availability. Most IMUs contain a magnetometer, as well as many common devices, including cellphones. Additionally, magnetometers have recently become cheaper and smaller.

The work explored in this dissertation indicates that an ambient magnetic field based navigation system can address and solve many indoor localization problems. An adapted SLAM system could serve as a solution for some domestic appliances (such as robot vacuum cleaners, for example). Furthermore, ambient magnetic field measurements could serve as a complement in a variety of navigation systems (such as in the context of robotic competitions, for example).

1.2 Objectives

The central objective of this dissertation is to demonstrate the possibility for a robot to resort to the inherent magnetic anomalies of an indoor environment, for navigation purposes. More precisely, the aim is to map the unique magnetic fingerprint of a two dimensional environment and correctly estimate the position of a mobile robot in the same environment, while resorting only to wheel odometry and magnetometer measurements. Moreover, the reliability and accuracy of the developed localization algorithm must be thoroughly tested with multiple experiments, including a Monte Carlo method.

In summary, the following tasks must be performed:

- Explore and apply the methods used to create a map of the environment's magnetic field.
- Create a localization algorithm that exploits the previously developed magnetic map and uses online measurements of the ambient magnetic field fused with odometry data to continuously estimate the position of a mobile robot on the mapped area.
- Present and compare results of multiple experiments performed to test the accuracy of the localization algorithm.
- Evaluate the reliability of the localization algorithm with a Monte Carlo method.

1.3 Document Outline

The remaining parts of the document are organized as follows:

- **Chapter 2:** Presents the state of the art of indoor localization in general, as well as some work regarding ambient magnetic field based localization.
- **Chapter 3:** Explains the processes and steps needed to map the magnetic field of the environment. Additionally, some theoretical concepts regarding magnetic field theory are introduced, as well as the employed hardware.

- **Chapter 4:** Describes the developed and implemented localization algorithm, based on a particle filter.
- **Chapter 5:** Presents and discusses the experimental results of the tests performed to evaluate the accuracy and reliability of the localization algorithm.
- **Chapter 6:** Presents the conclusions of the dissertation and explores some possibilities for future work.

CHAPTER 2

State of the Art of Indoor Positioning Systems

The focus of this chapter is to explore the state of the art of techniques and technologies used in real time localization systems nowadays. Firstly some techniques are introduced, followed by the technologies that apply some of them. Lastly, some research work regarding localization based on the ambient field is discussed.

2.1 Indoor Positioning Techniques

There are several positioning techniques that make use of one or more signal properties to estimate the position of sensor nodes. Positioning systems translate the signal properties into distances and angles, to then compute the actual position of a target object [1]. In this section, four techniques broadly used positioning techniques are addressed.

2.1.1 Time of Arrival (TOA)

In TOA based systems, the absolute time at which the signal arrives at the receiver is measured. A time stamped signal is emitted by a mobile node, and the signal's speed of propagation is used to convert the measured time into a distance. Each timestamp defines a circumference in the localization space on which the location of the mobile node lies. The intersection of multiple circumferences specifies the possible locations of the mobile node. TOA systems depend on the accurate synchronization of the arrival time of a signal transmitted from a mobile node to several receiving beacons [2]. This need for precise synchronization is one of the disadvantages of using this technique. Figure 2.1 illustrates the process behind TOA based systems.

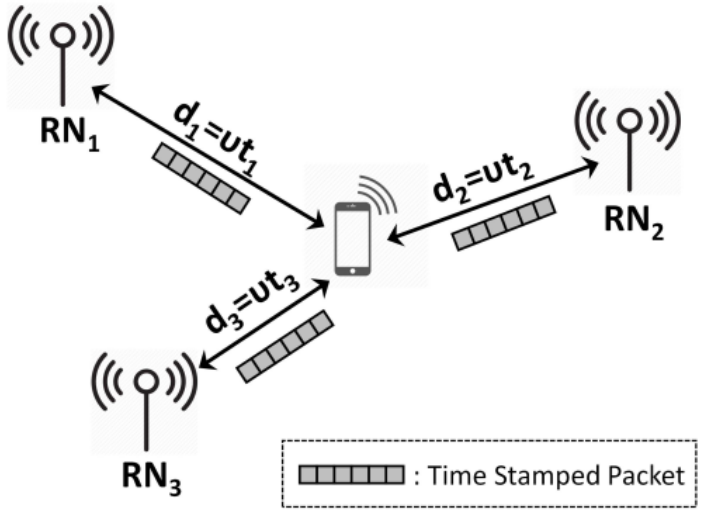

Figure 2.1: Usage of time stamped packets to measure distances in TOA based localization [3].

2.1.2 Time of Arrival Difference (TOAD)

Like TOA, TOAD systems are distance-based [1]. Multiple pairs of receiving nodes, with known positions, measure the relative time difference of signal arrival. Thus, there is no need for a synchronized time source of transmission in order to resolve timestamps, with only the receivers requiring time synchronization. Each difference of arrival time measurement produces a hyperbolic curve in the localization space on which the location of the mobile node lies. The intersection of multiple hyperbolic curves specifies the possible locations of the mobile node[2]. Figure 2.2 illustrates the process behind TOAD based systems.

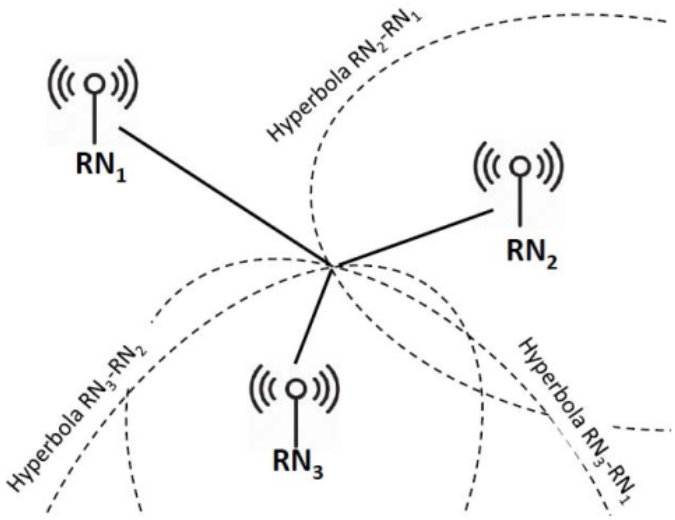

Figure 2.2: Intersection of hyperbolic curves to compute a position in TOAD based localization [3].

2.1.3 Angle of Arrival (AOA)

This technique uses the angle of arrival of the signal emitted by the mobile node, at multiple stationary receiving nodes of known location. While three or more receiving beacons can be used to improve accuracy, only two are need for 2D localization (except if the mobile node is located in the line that connects the two receiving beacons) [1]. AOA systems tend to be very accurate, but require complex and expensive hardware with highly directional antennas or antenna arrays. The amplitude or carrier-phase of the signal is compared across multiple antennas in order to estimate the target position. The result of this comparison is the intersection of the angle line from each signal source, which is then enables the computation of the receiver's triangulated position. Figure 2.3 illustrates the process behind AOA based systems.

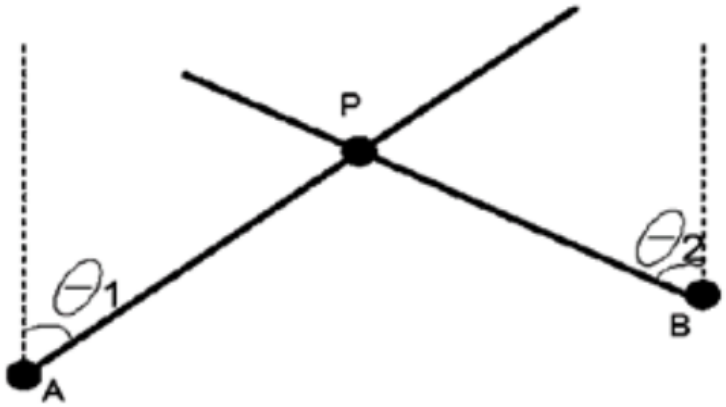

Figure 2.3: Intersection of angle lines from two signal sources to compute a 2D position in AOA based localization [3].

2.1.4 Received Signal Strength (RSS)

The methods previously addressed are either timing or angle based, which can be influenced by multipathing, decreasing the accuracy of the estimated position [2]. To counteract this issue, RSS can be used, where the distance from a mobile node to an access point is estimated by measuring the attenuation of the transmitted signal strength, due to propagation. This method is usually only applied with radio signals. A propagation model is used to convert the signal strength into a distance, as, generally, the received signal strength is inversely proportional to the distance [4]. Figure 2.4 illustrates the process behind RSS based systems.

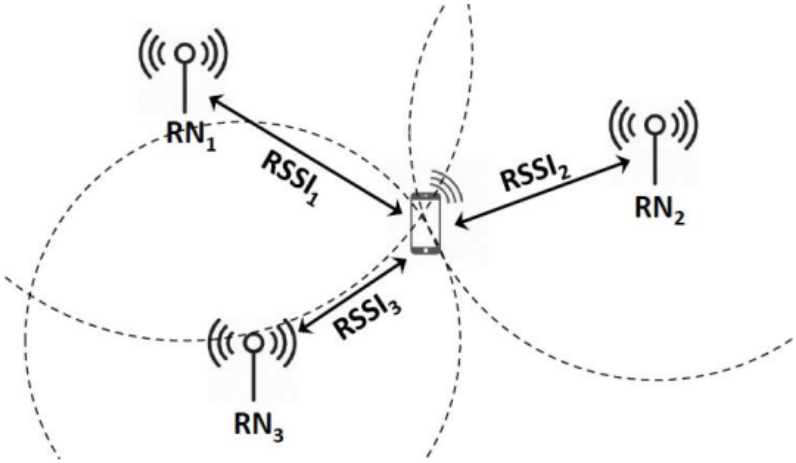

Figure 2.4: Conversion of signal strengths into distances to compute a position in RSS based localization [3].

2.2 Indoor Positioning Technologies

Positioning systems employ a variety of algorithms and techniques. Numerous technologies have been developed for navigation purposes, some of which employ the techniques previously addressed. In this section, some technologies widely used nowadays in indoor real time localization systems are presented.

2.2.1 Wireless Local Area Network (WLAN)

WLAN positioning systems use high frequency radio waves to communicate between nodes, that can be implemented with propagation and fingerprinting methods. The propagation method may use any of the signal properties presented in Section 2.1 to calculate the distances between the mobile and reference nodes needed for an appropriate positioning algorithm (usually trilateration), to compute the position of the mobile node [1].

One of the advantages of employing WiFi positioning systems is the compatibility with almost every WiFi device. Thus, eliminating the need for additional software installation or hardware manipulation. Beside this, while line of sight between sensors produces more accurate results, it is usually not a requirement in WLAN. Due to these advantages, WiFi positioning systems have become one of the most widespread approaches to solving indoor localization problems. [2].

2.2.2 Ultra Wideband (UWB)

UWB is defined as a RF signal occupying a portion of the frequency spectrum that is greater than 20 percent the value of the center carrier frequency, or has a bandwidth greater than 500 MHz [4]. UWB spreads the emitted information over a very large section of the frequency spectrum, allowing for a transmission that has both a high data rate and low power consumption.

The most common implementations of this technology use propagation methods, usually time of arrival (TOA) or time of arrival difference (TOAD), where an accuracy higher than 20 to 30 cm is required, which is not achievable through conventional wireless technologies (as is the case with wireless local area networks (WLAN) and radio frequency identification (RFID)). On the other hand, UWB is expensive and costly for a wide-scale implementation [2].

2.2.3 Ultrasonic

Ultrasonic positioning systems use sound waves at a frequency higher than the human hearing range, designated as ultrasounds. The most common applications of this technology use the time of arrival (TOA) of sound signals to estimate the distance between a mobile beacon (which emits the sound signal) and several reference beacons, of known location (which receive the sound signal). These distances are then computed through a localization algorithm (usually trilateration), to estimate the position of the mobile beacon.

However, the effects of noise and multipath effects usually degrade the accuracy and performance of large scale implementations. Also, the system becomes complex and costly when a large number of sensors is deployed. The need for a central server to compute the positions of the mobile nodes raises some privacy concerns [1]. Moreover, while there is not the issue of interference with other radio signals, no line of sight (NLOS) between nodes usually results in a significant decrease in accuracy.

Another approach to ultrasonic localization, is to place sonar transducers on the robot, as is shown in Figure 2.5. In these systems, the transducers emit an ultrasonic signal and the time of flight of the ultrasonic signal is measured (time between the signal's emission and the reception by the transducers). In essence, the distance between the robot's sonar and the physical obstacles in its line of sight is measured, which allows for a scanning of the environment (Figure 2.6). With a pre-built map and by employing a Kalman or particle filter, these systems can produce an accurate localization. The basis of sonar localization is similar to the LIDAR system used for ground truth positioning (presented in Chapter 3), in the sense that the time of flight of the signal is used to measure distances and produce a scan of the environment.

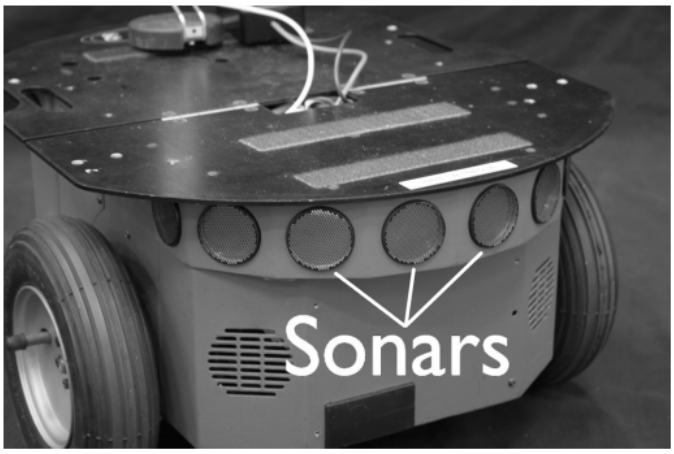

Figure 2.5: Sonar sensors placed on mobile robot [5]

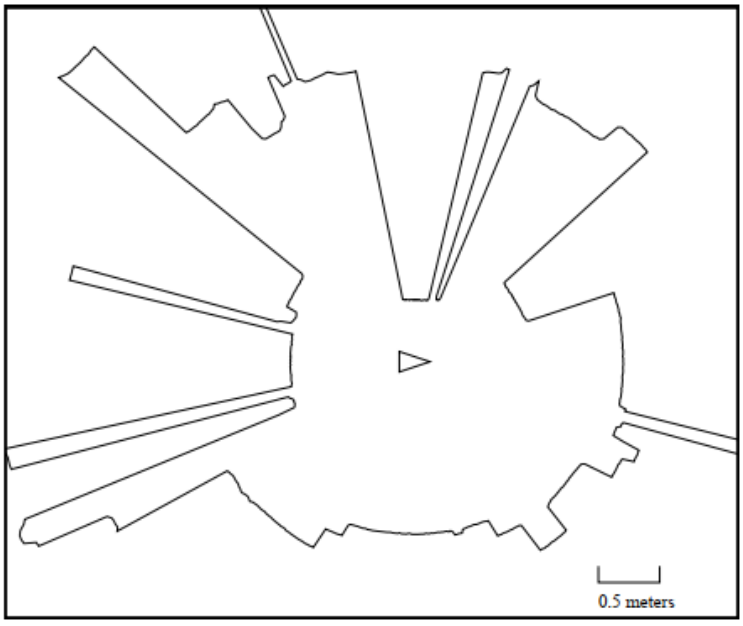

Figure 2.6: Typical sonar scan of an indoor environment [6]

2.2.4 Radio Frequency Identification (RFID)

RFID is a wireless technology that uses RF signals to establish communication between RFID tags and RFID readers. The reader queries and reads data from the tags, while each of the tags respond with an unique identification and stored information [1]. A tag can be classified as either active or passive. An active tag is powered by a battery, giving it a wider transmission range. A passive tag receives its power directly from the the reader's signal.

The RFID system itself can also be considered as active or passive, based on the types of the tags and the context in which they are used. In an active positioning system, the reader is mobile and the active tags are placed throughout the indoor environment. Since the active tags are battery powered and, hence, have a wider coverage area, fewer tags are needed to

cover the same area in an active positioning system. In a passive positioning system, the passive tags are placed throughout the indoor environment, usually resulting in a less costly solution, since passive tags are cheaper and do not need to be battery powered [1].

2.2.5 Scene analysis and miscellaneous systems

Besides the widely used technologies and techniques previously described, there are a number of different systems, also discussed in the literature, that rely on Infrared, ambient magnetic field, computer vision and a number of different technologies [3]. LIDAR and computer vision systems are widely used nowadays and often yield accurate and reliable results. The ground truth system presented in Chapter 3, is essentially based on processed LIDAR measurements. However, these solutions are usually costly and complex.

It is also important to note that most of the techniques presented up to this point, rely on fixed beacons or access points of known location (with the exception of the sonar system) that often have to be constantly powered. This is one of the advantages of scene analysis systems (as is the case of ambient magnetic field, sonar, LIDAR and vision based systems), that usually only require a navigation filter (and possibly a pre-built map), without any need for continuous use of beacons or access points.

2.3 Localization based on ambient magnetic field mapping

There already exists some work, with encouraging results, regarding 1D [7] and 2D [8] ambient magnetic field based localization. The work presented in [7] placed a magnetometer in a wheeled robot and uses the processed odometry data to obtain a ground truth position and maps the ambient magnetic field of a corridor. Then, the magnetometer is placed on a person who walks through the corridor, and the person's position and orientation is continuously estimated. A particle filter is employed and either the magnetic field vector norm $\|\boldsymbol{B}\|$, or the three vector components of the vector (B_x, B_y B_z), are used to estimated the person's orientation and position.

The more recent work presented in [8], uses a commercial motion capture system to provide an accurate 2D ground truth pose. A particle filter is employed and the magnetometer measurements are conjugated with either odometry data (in the case of non-legged locomotion) or inertial data (in the case of legged locomotion). The results presented in this article indicate a positioning error of less than 10cm, both when the magnetic field vector norm was used and when the full vector components were used.

CHAPTER 3

Magnetic Mapping

This chapter focuses on the procedures followed to produce a map of the ambient magnetic field of an indoor environment. Firstly, some concepts regarding electromagnetic theory are introduced. Secondly, the hardware specifications are presented, as well as some tests performed to validate the hardware's performance in the required circumstances. Finally, the actual practical procedures followed to map the magnetic field are presented, namely, the acquired data, the interpolation method and the validation of the generated map.

3.1 Magnetic Field Theory

Before addressing the methods used to create the magnetic map, some key concepts regarding electromagnetic and field theory are introduced. These concepts facilitate the understanding of all the work presented in this chapter and aid in contextualizing the aim of this dissertation. The material presented in this section is mostly based on the theory presented in Cheng (1989) [9], Jackson (1998) [10], Blakely (1996) [11], Serway and Jewett (2013) [12].

3.1.1 Vector Fields

In a vector field, each point in space is assigned a vector with a given magnitude and direction. To better explain this concept, an example is presented. Figure 3.1a shows an example of a two dimensional vector field, defined by Equations (3.1a) and (3.1b) [13]. In these circumstances, $\boldsymbol{F}(x, y)$ is always a unit vector at any point in space. This vector, when placed at the point (x, y), is a tangent vector to the circle centered at the origin that passes through (x, y), as is illustrated in Figure 3.1b [13].

$$\boldsymbol{F} : \mathbb{R}^2 \backslash 0 \rightarrow \mathbb{R}^2 \tag{3.1a}$$

$$\boldsymbol{F}(x, y) = \left(-\frac{y}{\sqrt{x^2 + y^2}}, \frac{x}{\sqrt{x^2 + y^2}} \right) \tag{3.1b}$$

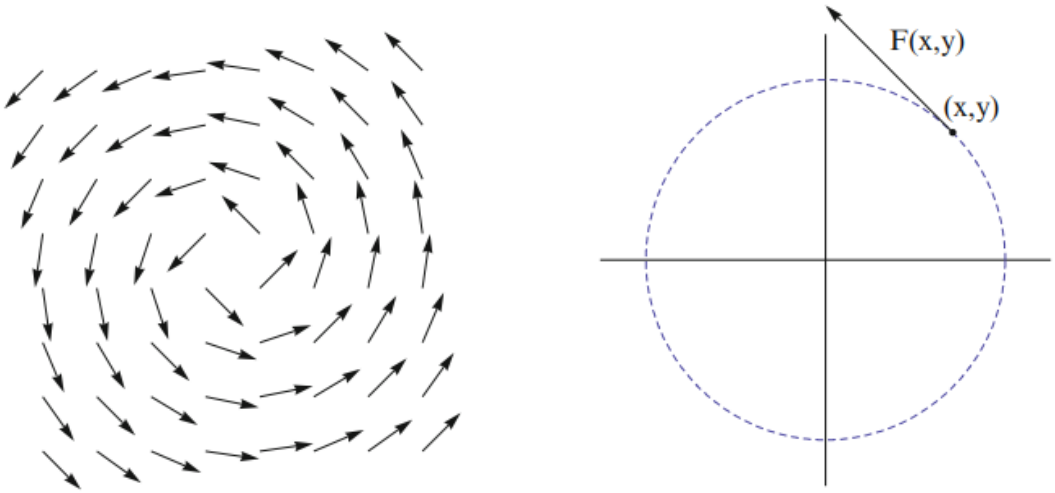

(a) Vector field at multiple points

(b) Vector field at a single point

Figure 3.1: Example of a vector field [13].

Any real magnetic field is a three dimensional vector field, usually defined by the vector valued function $\boldsymbol{B}(x, y, z)$, where any point in space has a vector with three components (B_x, B_y, B_z) associated to it. Next, two important two basic operations on vector fields are introduced; the divergence and the curl.

Divergence of a vector Field

The divergence is an operator, which operates on a vector field (or vector valued function) and outputs a scalar at each point in space. Given that $\boldsymbol{F}$ is a vector valued function, defined by Equation (3.2) (where $\hat{i}$, $\hat{j}$ and $\hat{k}$ are the standard unit vectors in the direction of the x, y and z axis, respectively), the divergence of $\boldsymbol{F}$, is defined by Equation (3.4). The conventional representation of divergence is presented in Equation (3.3).

$$\boldsymbol{F} = F_x\hat{i} + F_y\hat{j} + F_z\hat{k} \tag{3.2}$$

$$\nabla.\boldsymbol{F} \equiv \text{div}\boldsymbol{F} \tag{3.3}$$

$$\nabla.\boldsymbol{F} = \frac{\partial F_x}{\partial x} + \frac{\partial F_y}{\partial y} + \frac{\partial F_z}{\partial z} \tag{3.4}$$

An intuitive interpretation of divergence is that of a measure of how much the vector function spreads around a given point in space. A positive divergence indicates an "inward flow" towards that point, while a negative divergence value indicates an "outwards flow".

Curl of a vector Field

As is the case with divergence, the curl is also an operator which operates on a vector field, but, instead of a scalar, outputs a vector. Considering the same $\boldsymbol{F}$ function defined by Equation

(3.2), the curl of of $\boldsymbol{F}$, is defined by Equation (3.6). The conventional representation of divergence is shown in Equation (3.5).

$$\nabla \times \boldsymbol{F} \equiv \text{curl}\boldsymbol{F} \tag{3.5}$$

$$\nabla \times \boldsymbol{F} = \begin{vmatrix} \hat{i} & \hat{j} & \hat{k} \\ \frac{\partial}{\partial x} & \frac{\partial}{\partial y} & \frac{\partial}{\partial z} \\ F_x & F_y & F_z \end{vmatrix} = \left(\frac{\partial F_z}{\partial y} - \frac{\partial F_y}{\partial z}\right)\hat{\boldsymbol{\imath}} + \left(\frac{\partial F_x}{\partial z} - \frac{\partial F_z}{\partial x}\right)\hat{\boldsymbol{\jmath}} + \left(\frac{\partial F_y}{\partial x} - \frac{\partial F_x}{\partial y}\right)\hat{\boldsymbol{k}} \tag{3.6}$$

The curl vector at a certain point in a vector field, specifies the rotation around that point. The x component of the curl vector indicates the rotation in the yz plane, the y component indicates the rotation in the zx plane, and the z component indicate the rotation in the xy plane.

3.1.2 Scalar fields

In a scalar field, every point in space has a scalar value associated to it. Essentially, any vector field can be converted to a scalar by calculating the magnitude (or norm) of the vector at any point in space. Equation (3.7) shows a way to convert the three dimensional vector valued function $\boldsymbol{F}$ defined in Equation (3.2), to a scalar function f.

$$f = \|\boldsymbol{F}\| = \sqrt{F_x^2 + F_y^2 + F_z^2} \tag{3.7}$$

Figure 3.2 [14] shows the magnitude of the ambient magnetic field on a plane (a scalar field) that was generated from the three vector components of the magnetic field [14]. Next a basic operation performed on a scalar field is introduced, the gradient.

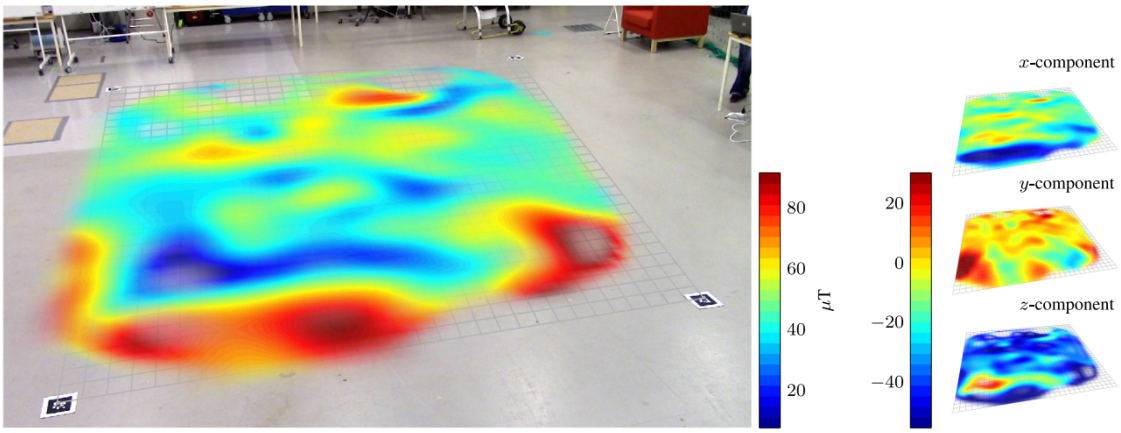

Figure 3.2: Magnitude of ambient magnetic field (left) and the respective magnetic field vector components (right). [14].

Gradient of a scalar field

The gradient is an operator, which, when operated on a scalar field, outputs a vector at each point in space. Given that f is a scalar valued function that operates in three dimensional space, the gradient of f is defined in Equation (3.9). The conventional notation used to represent the gradient of a function is presented in (3.8).

$$\nabla f \equiv \text{grad} f \tag{3.8}$$

$$\nabla f = \frac{\partial f}{\partial x}\hat{\mathbf{i}} + \frac{\partial f}{\partial y}\hat{\mathbf{j}} + \frac{\partial f}{\partial z}\hat{\mathbf{k}} \tag{3.9}$$

The gradient represents the main direction and rate of increase of the scalar field, for each point in space. The norm of the gradient indicates the net tendency of the scalar field in all directions.

3.1.3 Maxwell's Equations and Magnetostatics

Maxwell's Equations (3.10) are a set of coupled partial differential equations, that govern all electromagnetic phenomenon. In these equations, $\boldsymbol{E}$ represents the electric field, ρ is the charge density, $\boldsymbol{B}$ the magnetic field or magnetic flux density vector and $\boldsymbol{J}$ the current density. Furthermore, ε_0 is the permittivity of free space and μ_0 the permeability of free space.

$$\text{Gauss' Law} \qquad \nabla \cdot \boldsymbol{E} = \frac{\rho}{\varepsilon_0} \tag{3.10a}$$

$$\text{Gauss' Law } (\boldsymbol{B} \text{ Fields}) \qquad \nabla \cdot \boldsymbol{B} = 0 \tag{3.10b}$$

$$\text{Faraday's Law} \qquad \nabla \times \boldsymbol{E} = -\frac{\partial \boldsymbol{B}}{\partial t} \tag{3.10c}$$

$$\text{Ampere's Law} \qquad \nabla \times \boldsymbol{B} = \mu_0 \boldsymbol{J} + \mu_0 \varepsilon_0 \frac{\partial \boldsymbol{E}}{\partial t} \tag{3.10d}$$

To study magnetostatics (steady magnetic fields) in free space, one can disregard the eletric field $\boldsymbol{E}$ and only consider the magnetic flux density vector $\boldsymbol{B}$. The two fundamental postulates of magnetostatics that specify the divergence and curl of $\boldsymbol{B}$ in free space are presented in Equations (3.11) [9]. These equations were derived from Equations (3.10), based on the assumption that, in the stationary case, Maxwell's equations become decoupled and the terms $\frac{\partial \boldsymbol{E}}{\partial t}$ and $\frac{\partial \boldsymbol{B}}{\partial t}$ can be neglected. Equations (3.11) imply that the current density $\boldsymbol{J}$ is the source of the magnetic field $\boldsymbol{B}$. It is also important to note that Equations (3.11) presume that the changes in current density $\boldsymbol{J}$ are small enough to not be considered time dependant.

$$\nabla \cdot \boldsymbol{B} = 0 \tag{3.11a}$$

$$\nabla \times \boldsymbol{B} = \mu_0 \boldsymbol{J} \tag{3.11b}$$

3.1.4 Magnetic dipole moment

The magnetic field $\boldsymbol{B}$ at any point in space can be calculated by solving the systems of Equations (3.11) if the current density $\boldsymbol{J}$ is known. Alternatively, the magnetic field can be calculated by first calculating the magnetic dipole moment $\boldsymbol{m}$. In many scenarios of interest the current density is zero except in one small region V, as is shown in Figure 3.3 [15].

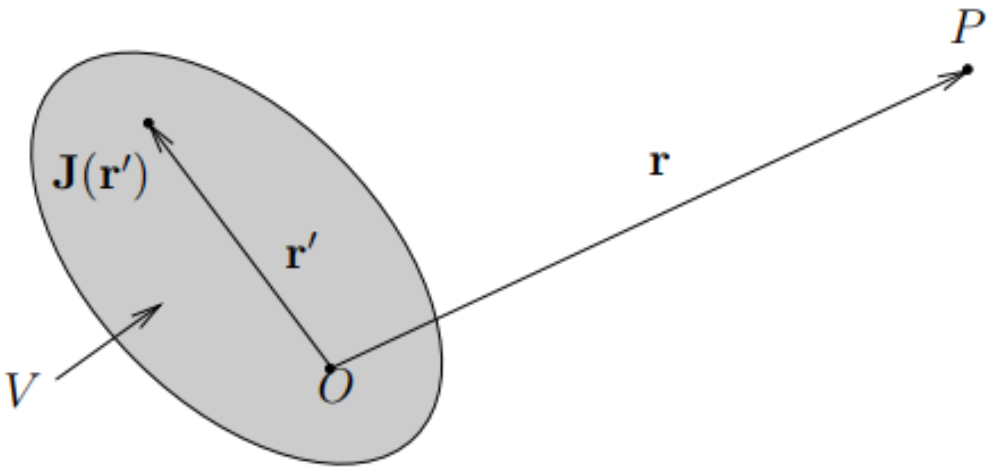

Figure 3.3: Localized current density in a region V resulting in a magnetic induction at point P [15].

The V region can be represented by its magnetic dipole moment ($\boldsymbol{m}$) at point O. In these circumstances, $\boldsymbol{m}$ can be calculated through Equation (3.12).

$$\boldsymbol{m} = \frac{1}{2}\int_V \boldsymbol{r} \times \boldsymbol{J}(\boldsymbol{r}) d^3\boldsymbol{r}\, dv \tag{3.12}$$

However, in the context of this work, the magnetic anomalies that distort the Earth's magnetic field are not usually caused by localized current densities. Instead, they are caused by magnetized ferromagnetic materials that can be represented by a magnetic dipole also have a given magnetic moment. In these circumstances the magnetic moment can be calculated in relation to the object's magnetization, as is presented in Equation (3.13), where $\boldsymbol{M}$ represents the magnetization field, V the volume of the object and dv the volume element. Figure 3.4 [14] illustrates how the Earth's magnetic field is distorted by a ferromagnetic object. These distortions are usually constant in time and are what create an unique magnetic fingerprint in many indoor environments. Sections 3.1.5 and 3.1.6 introduce some concepts regarding the properties of ferromagnetic materials and magnetization, respectively. It should also be noted that the magnetic anomalies caused by localized current densities may arise in indoor environments, but these may vary in time and would be undesirable in the context of the work presented in this dissertation.

$$\boldsymbol{m} = \iiint_V \boldsymbol{M}\, dv \tag{3.13}$$

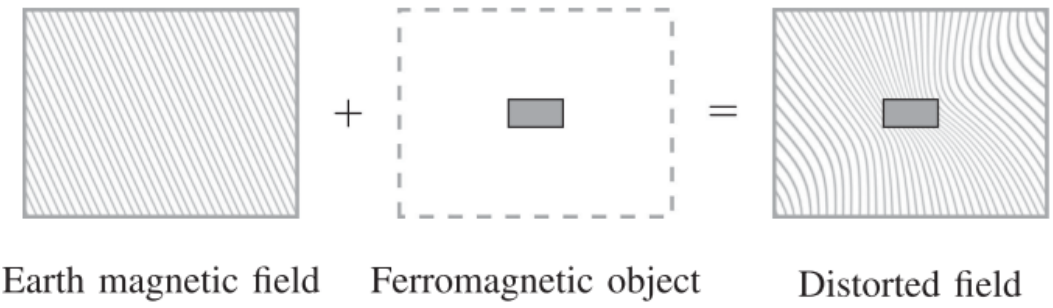

Figure 3.4: Distortion of the Earth's magnetic field, cause by a ferromagnetic object [14].

As can be inferred from Equation (3.14) , the strength of the magnetic field, caused by a dipole at a distance r, is inversely proportional to the cube of that same distance. Which implies that the strength of the magnetic field at a certain point in space, caused by a magnetic dipole, decays very rapidly when the point is moved farther away from the dipole. This aspect was taken into account when installing the magnetometer on the robot, as is described in Section 3.2.3. The magnetic moment of the dipole is represented by $\boldsymbol{m}$, and $\hat{\boldsymbol{r}}$ is the unit vector in the direction of $\boldsymbol{r}$.

$$\boldsymbol{B}(\boldsymbol{r}) = \frac{u_s}{4\pi}\left[\frac{\hat{\boldsymbol{r}}(\boldsymbol{m}.\hat{\boldsymbol{r}} - \boldsymbol{m})}{r^3}\right] \tag{3.14}$$

3.1.5 Ferromagnetic Materials

All electrons orbiting the atomic nuclei are spinnig on their axes, generating circular currents that effectively make them magnetic dipoles. The same applies to atomic nuclei, since these are positively charged and rotating. A given atom may not form a dipole, if the sum of the effects of its dipoles (caused by the electrons and atomic nuclei) cancel each other. On the other hand, if they do not cancel each other completely, then the atom will be a magnetic dipole, as is the case with ferromagnetic materials.

Ferromagnetic materials consist of permanent magnetic moments that tend to align parallel to each other even in weak magnetic fields. This alignment may persist, even after the external magnetic field is removed, and the material remains magnetized. This permanent alignment is due to a strong coupling between neighboring dipole moments. In an unmagnetized substance the atomic dipoles are randomly oriented, as is presented in Figure 3.5a. After an external magnetic field is applied, the atomic dipoles align themselves with the field, as is presented in Figures 3.5b and 3.5c [12]. When the external field is removed, the sample may retain a net magnetization in the direction of the original field.

These ferromagnetic materials are the main reason for the distortion of the earths magnetic field that is often observed in indoor environments. There are some other factors that induce magnetic anomalies, namely wires that carry an electric current (although these anomalies are usually not static in time and may actually damage the performance of the localization algorithm).

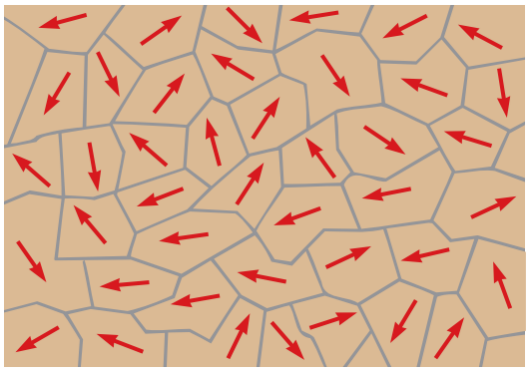

(a) Unmagnetized substance.

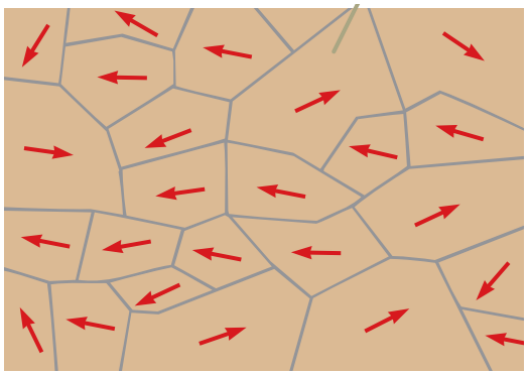

(b) Substance after a magnetic field is applied.

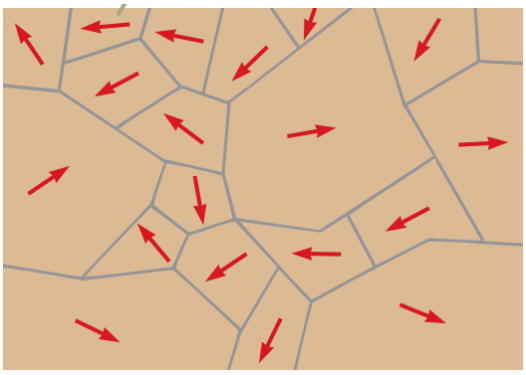

(c) Substance after a stronger magnetic field is applied.

Figure 3.5: Orientation of magnetic dipoles of a ferromagnetic substance, before and after a magnetic field is applied [12].

3.1.6 Magnetization

Considering that any orbiting electron can be represented by a magnetic dipole with magnetic moment $\boldsymbol{m_i}$, if there are n atoms per unit of volume, the magnetization can be defined by Equation (3.15). Where $\sum_{i=1}^{n\Delta V} \boldsymbol{m_i}$ represents the sum of all magnetic dipole moments with the volume element ΔV, centered at $\boldsymbol{r}$.

$$\boldsymbol{M}(\boldsymbol{r}) = \lim_{\Delta V \to 0} \frac{\sum_{i=1}^{n\Delta V} \boldsymbol{m_i}}{\Delta V} \tag{3.15}$$

This definition, indicates that magnetization can be considered as a density of magnetic dipole moments and allows for the description of complex magnetized regions without using a large number of magnetic dipole moments [15].

3.2 Hardware used in this dissertation

The aim of this section is to describe and justify the use and placement of some key sensors, as well as the robot used in the context of this work. For this purpose the hardware specifications are presented, as well as some tests performed to validate them.

3.2.1 Magnetometer

The magnetometer used in the work presented in this dissertation was the one incorporated in the MTi-30 AHRS, which is a full gyro-enhanced Attitude and Heading Reference System (AHRS), manufactured by Xsens. It gives various outputs: drift-free roll, pitch and true/magnetic North referenced yaw, plus sensor measurements: 3D acceleration, 3D rate of turn and 3D earth-magnetic field data. Although, in this work, only the 3D magnetic field data was considered. The output of the magnetometer is in arbitrary units (a.u.), where one a.u. is the magnetic field strength during calibration at Xsens calibration lab. This is approximately 40 uT. [16]

Figure 3.6 shows a plot of the data acquired with the MTi-30 AHRS in a fixed position, through a period of 24 hours at a sampling frequency of 1 Hz. The mean value of the measurements is 1.241 a.u. and the variance is 2.611e-5 a.u.^{2}. The value of the lowest measurement was 1.205 a.u., while the value of the highest measurement was 1.275 a.u. Nevertheless, it can be inferred from Figure 3.6 that most measurements belong to a range of approximately 1.225 to 1.260 a.u. All these results are summarized in Table 3.1. This acquisition indicated that the MTi-30 AHRS has a good enough precision for the context of this work. As will be addressed in Section 3.3, the norm of the magnetic field vector measurements taken while mapping a large area, lied between 0.018 a.u. and 5.275 a.u.

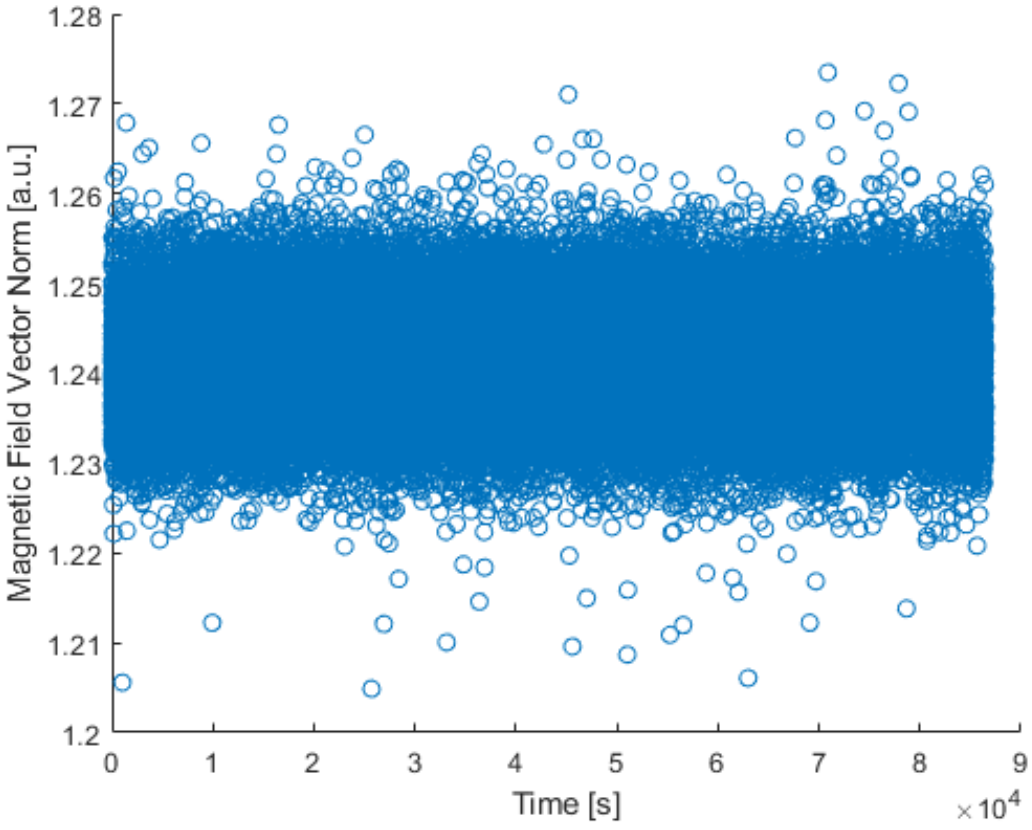

Figure 3.6: Acquisition with a fixed MTi-30 AHRS during a 24 hour period.

Statistic	Value
Mean value	1.241 a.u.
Standard deviation	5.110e-3 $a.u.$
Variance	2.611e-5 $a.u.^2$
Maximum value	1.275 a.u.
Minimum value	1.205 a.u.
Range where more than 99% of the measurements lie	1.225 a.u. to 1.260 a.u.

Table 3.1: Statistics of acquisition with a fixed MTi-30 AHRS during a 24 hour period.

3.2.2 LIDAR

Both for mapping the ambient magnetic field and validating the developed localization algorithm, an accurate ground truth positioning system is essential. For this purpose, the LMS100 2D LIDAR sensor was used. This sensor was developed to measure distances and scan indoor environments. The raw data outputed by the LIDAR was processed and supplied to a navigation algorithm, in order to provide an accurate estimation of the robot's current pose. Figure 3.7a shows a photo of the sensor and Figure 3.7b illustrates its range. More detailed information regarding the LMS100 can be found in the product's data sheet [17].

(a) Photo of the LMS100 used for ground truth positioning [17]

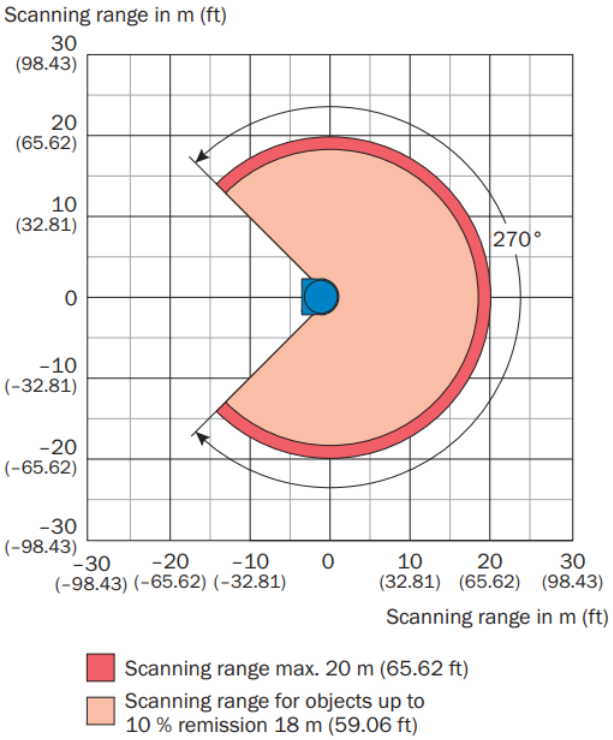

(b) LMS100 range [17]

Figure 3.7: LMS100 photograph and range illustration [17]

3.2.3 Robot

The robot and sensors used throughout this work are presented in Figure 3.8. Figure 3.8b shows two IMUs installed on the robot, each with a magnetometer (which was the only component of the IMU that was used). The data acquired with the bottom IMU was used for localization purposes, while the data acquired with top IMU was used to validate the continuation of the magnetic field to different heights (which is not in the scope of the work presented in this dissertation). Figure 3.8c shows the LIDAR installed on the robot.

The robot's structure is made out of aluminum, which is a non-ferromagnetic material. Nevertheless, the structure may cause some distortion of the ambient magnetic field, since it is an electrically conductive material and can generate induced currents in the presence of strong electromagnetic fields. Furthermore, ferromagnetic impurities may be present in the aluminum alloy.

The magnetometer has been placed sufficiently far from the vehicle body and other sources of electromagnetic noise, such as engines, in order to mitigate those inferences. In the performed tests, with the robot in different orientations and in motion, no significant changes were observed in the magnetic field measured by the magnetometer installed in the robot, so it is assumed that there are no distortions caused by the vehicle. Moreover, since the environment was an open field (Figure 3.9), the bottom IMU was placed as close to the ground has possible, ensuring that it was the closest to the magnetic anomalies caused by the ferromagnetic structures bellow the building's floor.

The robot has four omnidirectional wheels. Each wheel has an encoder that measures the angular velocity of the wheel. The encoder measurements (also referred as odometry measurements) are then processed to give a dead reckoning estimation of the robot's pose.

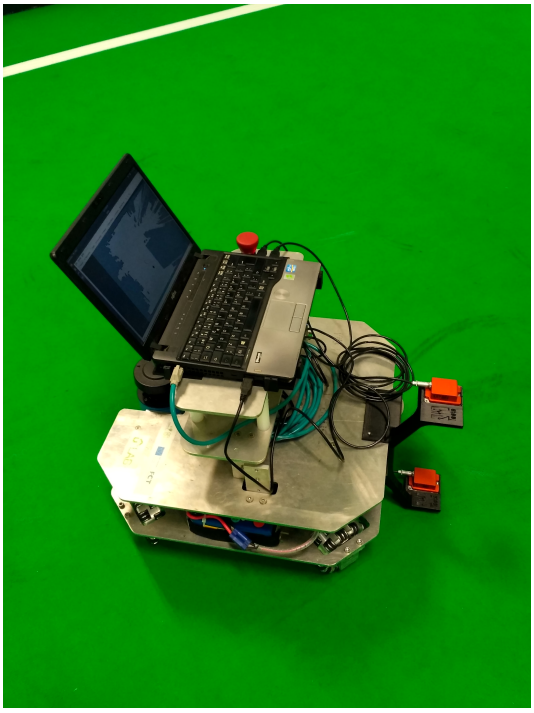

(a) Side picture of the robot.

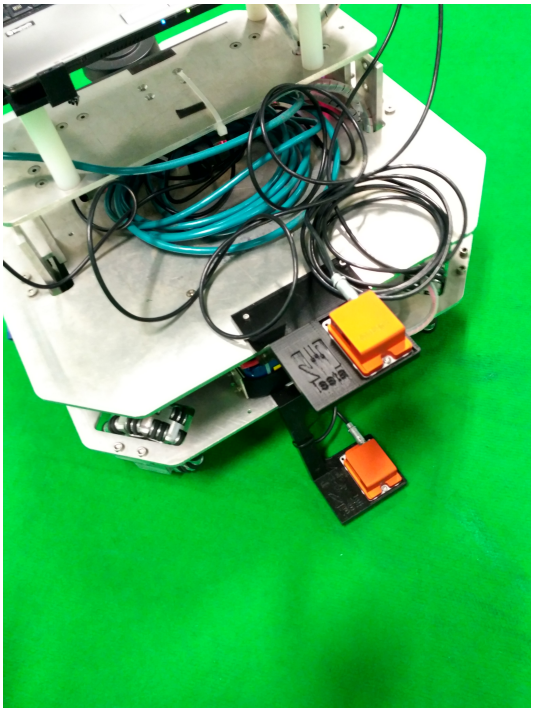

(b) The two IMUs (only the bottom one was used).

.

.

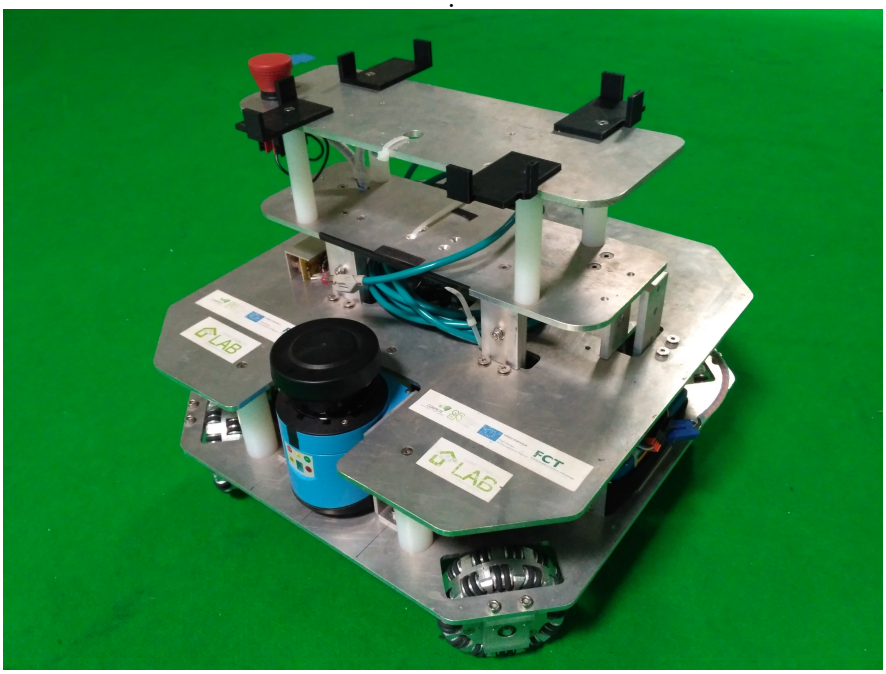

(c) Robot and installed sensors.

Figure 3.8: Robot and installed sensors.

Figure 3.9: Mapped environment from three perspectives.

Along the whole data acquisition process, there were three key values that were registered: the wheel odometry measurements, the ground truth position and the magnetometer measurements. All these measurements were synchronized and acquired at a sampling frequency of 50 Hz.

The odometry measurements were processed to give a dead reckoning estimate of how much the robot moved since the last iteration and its change in orientation. The odometry measurements at a given time t are represented by the vector $\boldsymbol{U_t}$, with the following components: U_x, U_y (the difference in position in meters) and U_θ (the difference in orientation in radians).

The ground truth pose was acquired with a navigation algorithm that used the LIDAR measurements to provide an accurate estimation of the robot's current position and orientation. The ground truth pose is represented by the vector $\boldsymbol{X_t}$, with the following components: x, y (the robot's current position in meters) and θ (the robot's current orientation in radians).

The magnetometer measurements provided the ambient magnetic field vector at the current location of the magnetometer. This vector is represented by $\boldsymbol{Z_t}$ and is composed by its three spacial components (Z_x, Z_y, Z_z) in arbitrary units. In the context of this dissertation, only the magnetic field vector norm $\|\boldsymbol{Z_t}\|$ was considered. Table 3.2 summarizes the units and the notation used for these key measurements.

Description	Vector	Components	Units
Odometry	$\boldsymbol{U_t}$	(U_x, U_y, U_θ)	meters and radians
Ground Truth	$\boldsymbol{X_t}$	(x, y, θ)	meters and radians
Magnetic Field	$\boldsymbol{Z_t}$	(Z_x, Z_y, Z_z)	arbitrary units (a.u.)

Table 3.2: Key measurements registered during acquisition.

Even though the odometry data was registered in all acquisitions, it was not used in the acquisitions for mapping and map validation purposes. The odometry data was only used in the navigation experiments (presented in Chapter 5), where the aim was to determine the robot's position, using only the odometry and magnetic field data.

Since the position of the magnetometer relative to the robot's frame is fixed, to compute the absolute position of the magnetometer $\boldsymbol{X_m}$ in the global frame, its 2D coordinates in the robot referential frame (x_r, y_r) are rotated using the rotation matrix $\boldsymbol{R}$ defined in Equation(3.16a). The $\boldsymbol{R}$ matrix is parameterized by the ground truth orientation angle (θ) and added to the 2D coordinates of the robot expressed in the global frame, as is shown in Equation (3.16b).

$$\boldsymbol{R} = \begin{bmatrix} \cos\theta & -\sin\theta \\ \sin\theta & \cos\theta \end{bmatrix} \tag{3.16a}$$

$$\boldsymbol{X_m} = \begin{bmatrix} x \\ y \end{bmatrix} + \boldsymbol{R} \cdot \begin{bmatrix} x_r \\ y_r \end{bmatrix} = \begin{bmatrix} x + x_r\cos\theta - y_r\sin\theta \\ y + x_r\sin\theta + y_r\cos\theta \end{bmatrix} \tag{3.16b}$$

The mapped area has dimensions of 11.5m by 8.9m. Figure 3.10 presents the trajectory performed by the magnetometer during the acquisition used to map the environment. The mobile robot was controlled remotely and manually, while trying to follow a pre-defined path in the form of a lawn-mower trajectory in order to obtain a dense coverage of the area. Figure 3.11 presents the norm of the magnetic field vector acquired during the same trajectory. It should be noted that the vertical lines (parallel to the ordinate axis) were performed first, followed by the horizontal lines (parallel to the abscissa axis) that intersect the vertical lines. The maximum and minimum magnetic intensity measurements acquired in this phase were 5.275 a.u.and 0.018 a.u, respectively.

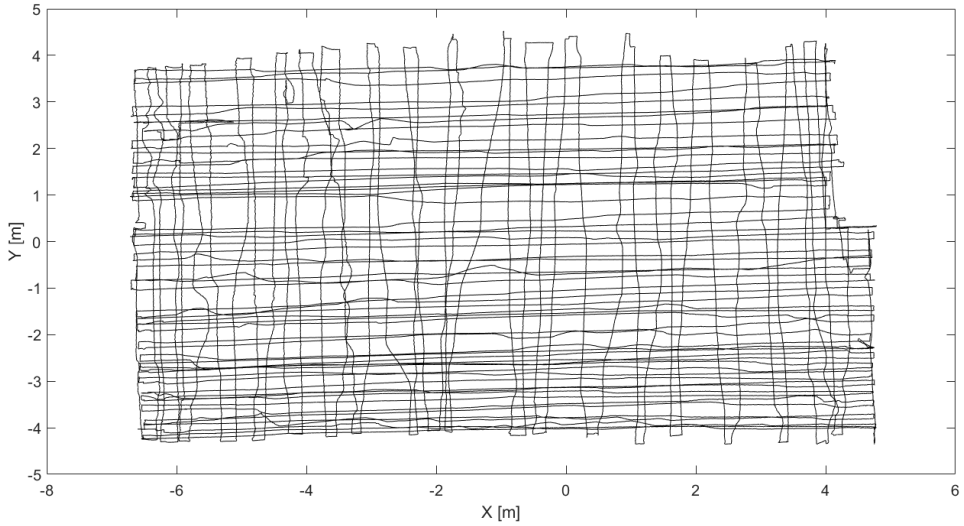

Figure 3.10: Robot's trajectory while acquiring data to map the testing area.

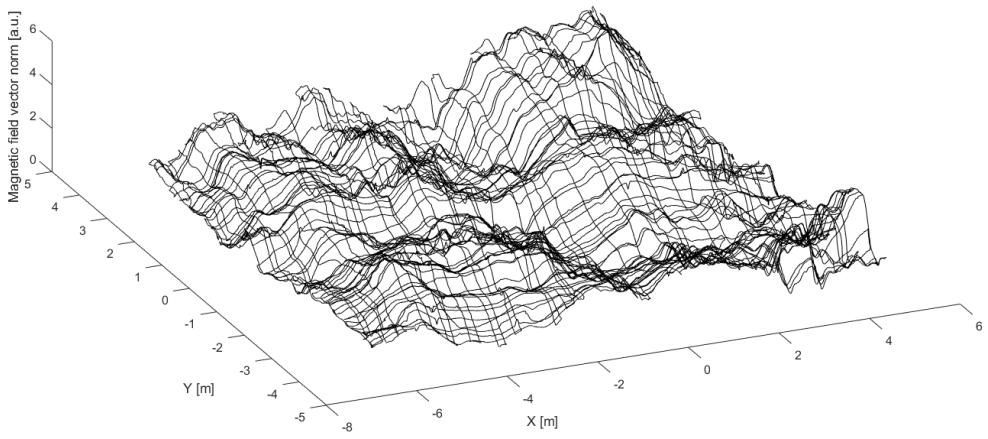

Figure 3.11: Magnetometer measurements throughout mapping trajectory.

3.3.1 Validation of acquisition

To validate the acquisition, the measurements taken in the same region, but at separate times, were compared and verified to have similar values. The colored dots in Figure 3.12 represent the intersections in the robot's mapping trajectory. The color spectrum indicates the absolute difference between the two measurements taken at each intersection at different times. Between most of the samples that are compared at each intersection, a significant amount of time has passed and the robot has covered a considerable distance. Since the acquisition was performed with a sampling rate of 50Hz and the speed of the robot was considerably slow (when compared with the sampling frequency), the samples compared at each intersection were sufficiently close to each other.

Considering the 2382 intersections registered, the mean of the absolute difference at each intersection was 0.031 a.u. This value is within the uncertainty of the MTi-30 AHRS, reviewed in Section 3.2.1. The maximum absolute difference was 0.192 a.u. and only 32 intersections registered a an absolute difference higher than 0.1 a.u.

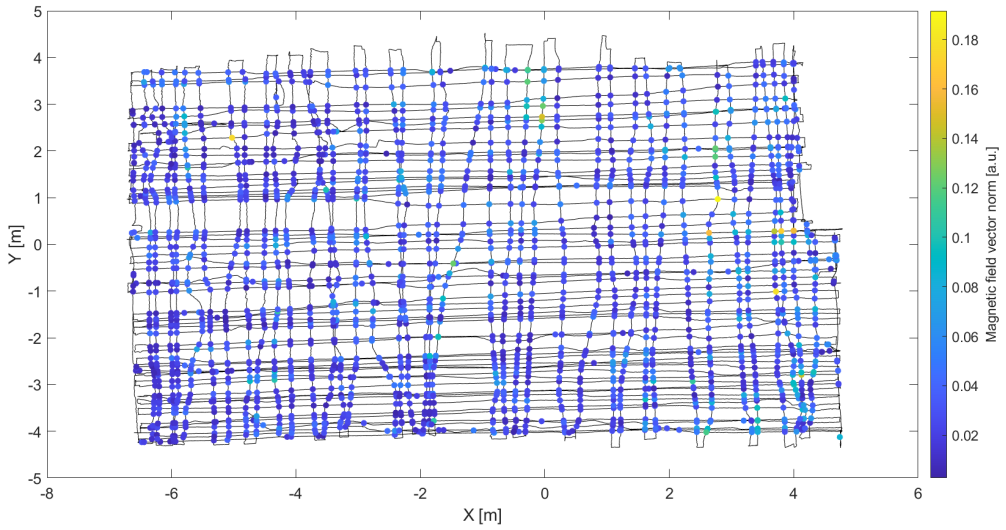

Figure 3.12: Mapping trajectory with coloured dots representing the registered intersections where the magnetometer measurements were compared. The color spectrum indicates the absolute difference between the two measurements taken at each intersection.

3.4 Magnetic Data Interpolation

With the acquired data presented in the last section, the next step was to interpolate the data to a grid of points regularly distributed throughout the map. The points where the magnetic field vector norm was interpolated formed a 0.02m by 0.02m square grid, throughout the entirety of the map.

The computational method used to interpolate the data was ordinary Kriging. Kriging is a geostatistical interpolation method that uses the spatial correlation of the distance and direction between the points where measurements have been taken (often called sample points

and whose value is represented by Z_s). The value at the interpolated points (also called grid points, in this context, whose value is represented by Z_g) are calculated through Equation (3.17) [18].

$$Z_g = \sum_{n=1}^{N} w_k[n] Z_s[n] \tag{3.17}$$

The value interpolated at each grid point is based on the values at the sample points in the search area near the grid point. This search area is usually delimited by a circumference with a specified radius, with its center on the grid point. In the performed interpolation, a radius of 7.1 meters was used. In this context, w_k denotes the weights that are multiplied by the value at the sample points to estimate the value at the grid points. Thus, each sample point in the search neighborhood of a certain grid point, has a specific weight, whose value is usually inversely proportional to the distance between the the sample and grid points. The higher the weight of a sample point, the more influence its value will have on estimating the value of the grid point.

In order to optimize the interpolation, the weights used in this method must be computed from variograms (or semi-variograms). A variogram is a mathematical model of the continuity of spatial data. Figure 3.13 presents a variogram of the acquired data. The abscissa axis of the variogram is the lag distance, which represents the distance between each of the sample points. The Y axis represents the average absolute difference (in a.u.), for each lag distance. To obtain a variogram function, the data must be fitted to a defined function. In this case, a spherical fitting was employed, with a scale of 0.6 and a length of 2.1 meters.

The weights for each sample point are calculated through equation (3.18), where A is a matrix comprised of variogram functions between each of the sample points in search area, and b is a vector, also comprised of variogram functions, but between the grid point and the sample points in the search area. Equation (3.19) shows the composition of the matrices, where x_1 to x_n are the grid points in the search neighborhood, x_0 is the grid point, γ is the variogram function and μ the Lagrange parameter [18].

$$Aw_k = b \quad <=> \quad w_k = A^{-1}b \tag{3.18}$$

$$\begin{bmatrix} w_{k_1} \\ \vdots \\ w_{k_n} \\ \mu \end{bmatrix} = \begin{bmatrix} \gamma(x_1 - x_1) & \dots & \gamma(x_1 - x_n) & 1 \\ \vdots & \ddots & \vdots & \vdots \\ \gamma(x_n - x_1) & \dots & \gamma(x_n - x_n) & 1 \\ 1 & \dots & 1 & 0 \end{bmatrix}^{-1} \begin{bmatrix} \gamma(x_1 - x_0) \\ \vdots \\ \gamma(x_n - x_0) \\ 1 \end{bmatrix} \tag{3.19}$$

Figures 3.14 and Figure 3.15 show the surface and contour maps, respectively, of the interpolated maps. As can be observed in the contour map of Figure 3.15, there are some linear alignments of magnetic anomalies that traverse the whole mapped area. These features, which

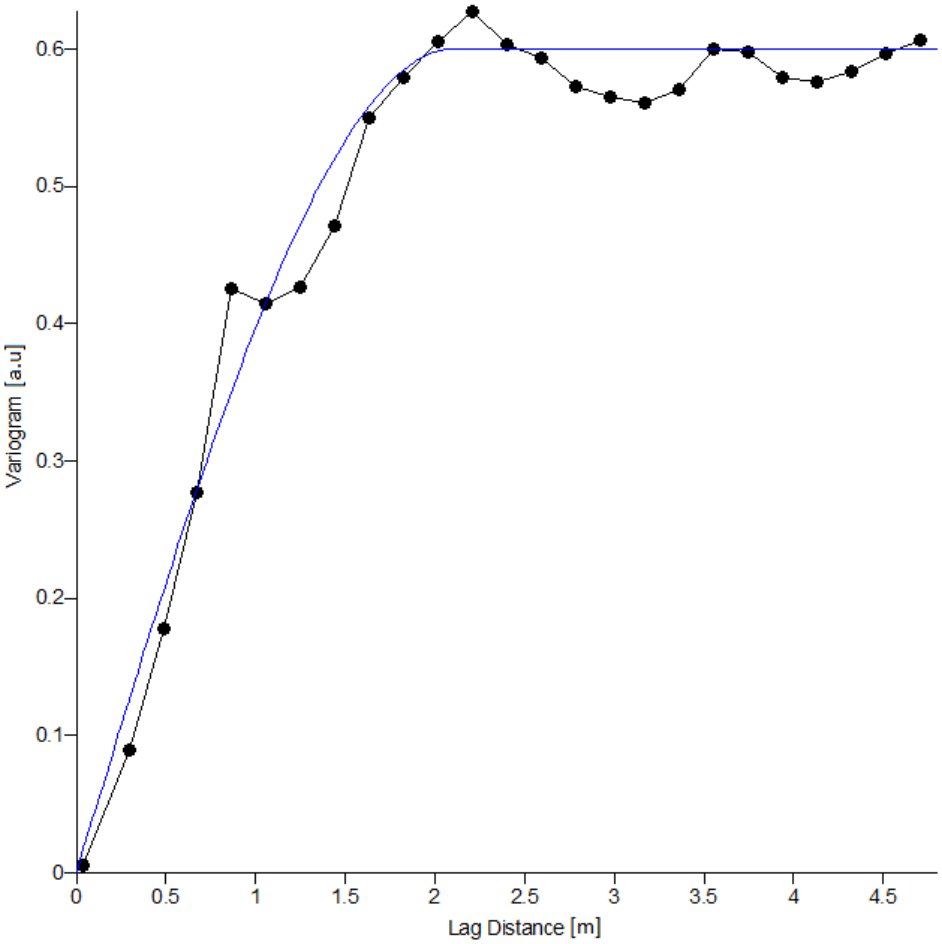

Figure 3.13: Variogram of mapping acquisition with spherical fitting.

initially were suspected to be artifacts introduced by some deficiency in the signal processing of the magnetic data, were finally identified as being originated by building structures underlying the pavement of the indoor environment. Thus, instead of constituting undesirable artifacts, these are useful features from the point of view of magnetic navigation because they constitute important sources of information in terms of localization.

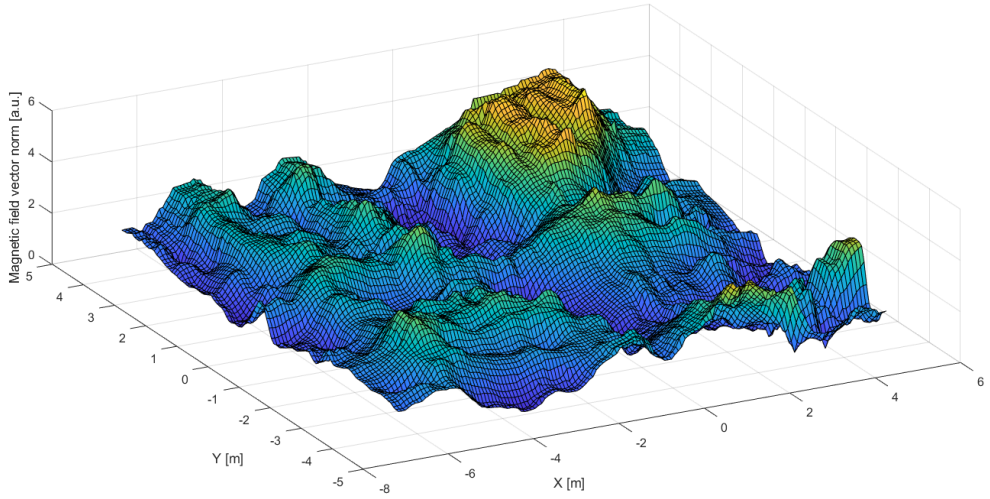

Figure 3.14: Magnetic surface map of interpolated data.

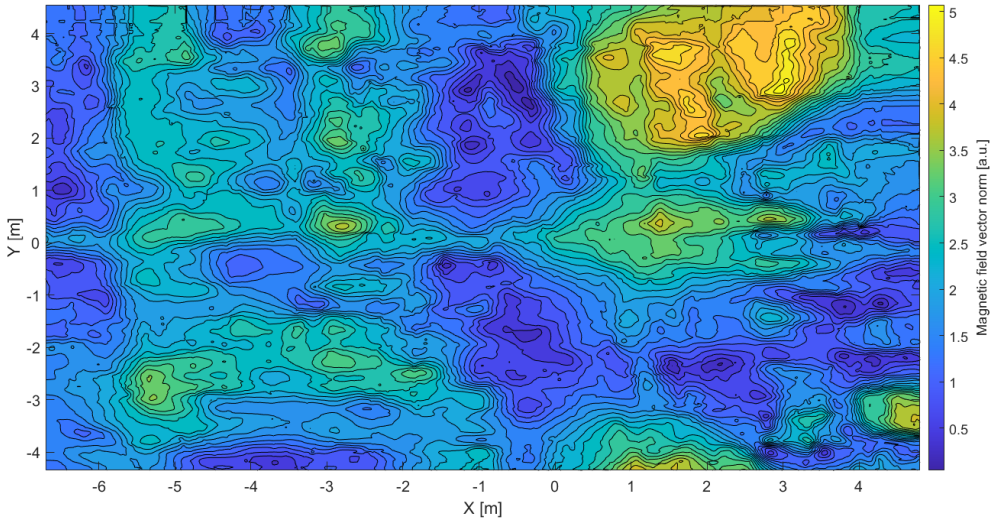

Figure 3.15: Magnetic contour map of interpolated data.

3.4.1 Validation of interpolation

To validate the quality of the interpolation, additional data was acquired on some of the interpolated regions, after the interpolation had already been performed. The colored dots in Figure 3.16 represent the samples taken in three separate trajectories. The color spectrum indicates the absolute difference between the measured value of each sample and the interpolated value at the position of that same sample.

As was already mentioned, the map was interpolated to a 0.02m by 0.02m square grid. To obtain an interpolated value at the position of each of the sample points of the post mapping trajectories, a bilinear interpolation was applied, using the four closest grid points. Figure 3.17 and Equation 3.20 show how the magnetic filed at a point (x_p, y_p) is estimated using bilinear

interpolation, where the four closest grid points are: (x_1, y_1), (x_1, y_2), (x_2, y_1), (x_2, y_2).

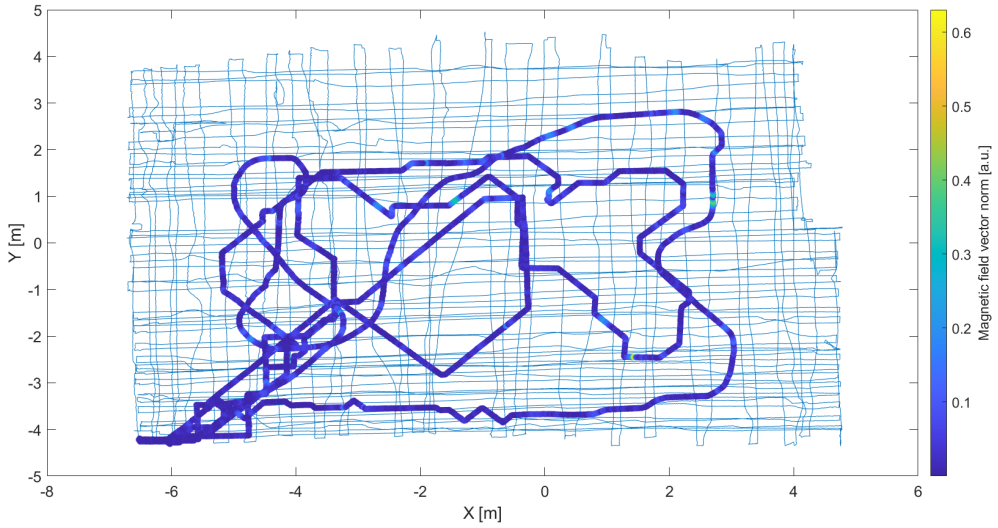

Figure 3.16: Validation of the interpolated map by comparing the data acquired in three separate trajectories with the interpolated data. The colored dots represent the samples taken in three separate trajectories. The color spectrum indicates the absolute difference between the measured value of each sample and the interpolated value at the position of that same sample.

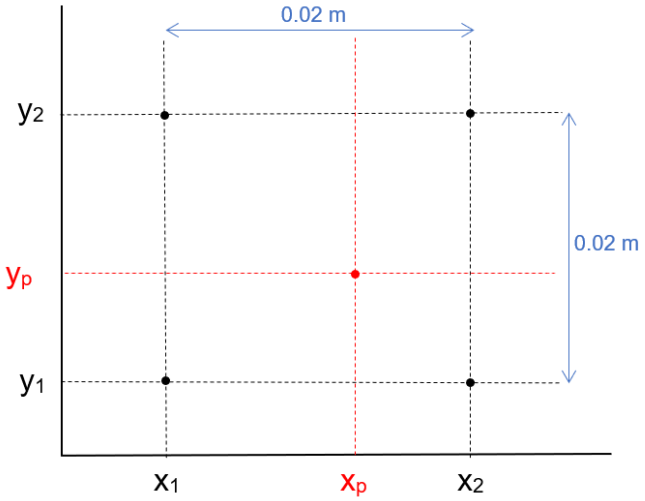

Figure 3.17: Bilinear interpolation of point (x_p, y_p).

$$f(x_p, y_p) \approx \frac{1}{(x_2 - x_1)(y_2 - y_1)} \begin{bmatrix} x_2 - x_p & x_p - x_1 \end{bmatrix} \begin{bmatrix} f(x_1, y_1) & f(x_1, y_2) \\ f(x_2, y_1) & f(x_2, y_2) \end{bmatrix} \begin{bmatrix} y_2 - y_p \\ y_p - y_1 \end{bmatrix} \tag{3.20}$$

Considering the 21334 samples, the mean of the absolute difference between the interpolated and acquired values was 0.0262, which is within the uncertainty of the magnetometer. The

maximum absolute difference was 0.630 a.u. While most values are within the uncertainty of the magnetometer, some of the greater registered discrepancies are due to measurements taken where the gradient of the magnetic filed is higher, where errors in the ground truth positioning often result in a greater difference between the interpolated and acquired magnetic field intensity values.

Table 3.3 summarizes some of the results presented throughout this chapter.

Statistic	**Value**
Standard deviation of acquisition with a static magnetometer through a 24 hour period	5.110e-3 $a.u.$
Variance of acquisition with a static magnetometer through a 24 hour period	2.611e-5 $a.u.^2$
Range of measurements acquired during mapping trajectory	0.018 a.u to 5.275 a.u
Mean of absolute difference registered in validating the acquisition	0.0311 a.u.
Standard deviation of absolute difference registered in validating the acquisition	0.0221 a.u.
Variance of absolute difference registered in validating the acquisition	4.869e-04 $a.u.^2$
Mean of absolute difference registered in validating the interpolation	0.0262 a.u.
Standard deviation of absolute difference registered in validating the interpolation	0.0347 a.u.
Variance of absolute difference registered in validating the interpolation	1.207e-3 $a.u.^2$

Table 3.3: Statistics of results from mapping phase.

CHAPTER 4

Magnetic-based Localization using Particle Filters

This chapter focuses on the process of developing a localization algorithm, based on a particle filter. The role of the algorithm is to continuously estimate the robot's position, while the robot is performing an arbitrary trajectory on the mapped area presented in Chapter 3. For this purpose, the magnetometer is constantly measuring the ambient magnetic field and the real time odometry data is being registered.

To describe the localization process, first, some general concepts regarding particle filtering are introduced. Subsequently, the operation of the actual implemented algorithm is described. The material presented in this section is generally based on the theory presented in Thrun (2000) [19]. Some concepts and operations employed more specific to the implemented algorithm were based on the work presented in [20] and [21].

4.1 Essential aspects and properties of a particle filter

The particle filter is a non-parametric filter that can approximate a broad range of statistical distributions, as opposed to parametric filters, which usually assume normal Gaussian distributions. The filter's estimation of the target value is done via a finite number of generated values, each corresponding to a specific position in space [19].

4.1.1 Notation

Table 4.1 describes the notation used throughout this section. Some of the notation coincides with the notation used in previous chapters, but has a different meaning in the context of this chapter. In Chapter 3, X_t represented the current ground truth pose, where as here it represents the current state. Also in Chapter 3, Z_t represented the full magnetic field vector acquired by the magnetometer, where as here it represents the magnetic field vector norm.

Notation	Description
X_t	State at time t
$\hat{X}_t$	Predicted state at time t
$X_t^{[i]}$	State given by the particle i at time t
$\hat{X}_t^{[i]}$	Predicted state given by the particle i at time t
Z_t	Measurement at time t
$\hat{Z}_t$	Predicted measurements at time t
$\hat{Z}_t^{[i]}$	Predicted measurements associated to the particle i at time t
$\bar{X}_t$	State estimate at time t
$w_t^{[i]}$	Weight of particle i at time t
$f(.)$	Motion model
W_t	Noise of the motion model
U_t	System's inputs at time t
$g(.)$	Measurement model
V_t	Noise of the measurement model
N	Number of particles
N_{eff}	Effective number of particles
T_{eff}	Resampling threshold
σ_z	Standard deviation of measurement error
σ_u	Standard deviation of motion model error
σ_i	Standard deviation of initial particle distribution
μ_i	Mean of initial particle distribution
d_m	Minimum distance the robot must travel to enter a new iteration

Table 4.1: Notation used to describe the operation of the particle filter.

4.1.2 Particle definition

The particles are defined as a collection of data, which represent a probability distribution of the system's states, within the state space of the system. Essentially, each particle represents a possible state $X_t^{[i]}$, with a given weight $w_t^{[i]}$ (which is related to the probability of that particle representing the real current state of the system). The set of all particles at an instant t, defined as ${X_t^{[i]}}_{i=1}^{N}$, describes the probability distribution of all the states at that instant. In the context of this work, the state of each particle $X_t^{[i]}$ represents a possible position on the mapped environment.

4.1.3 Motion model

A particle filter must be based on a motion model, represented by the f function, which defines how the system evolves through time. The motion model depends on the following aspects:

- The previous state X_{t-1}.
- The system's inputs, also called control variables and represented by the vector U_t. In the context of this work, U_t depicts the processed odometry measurements.
- The noise of the system, which includes: the noise of the process model, the input noise and the disturbances (noise external to the system). For simplification purposes, all

these sources of noise can be represented by a single noise variable W_t.

4.1.4 Measurement model

The measurement model, represented by the g function, defines the measurements Z_t acquired by the system, based on its current state X_t. The measurements are affected by the measurement noise V_t, which is sampled from a Gaussian distribution with mean equal to zero and standard deviation σ_z. In the context of this work, the g function corresponds to the magnetic map, parameterized by the robot's current position X_t. The measurement Z_t represents the current magnetic field measurement acquired by the magnetometer. Equation(4.1) shows how the current measurement is determined, based on the measurement model and the current state.

$$Z_t = g(X_t) + V_t \quad \text{with} \quad V_t \sim \mathcal{N}(0, \sigma_z) \tag{4.1}$$

4.2 Particle filter operation

The basic operation of a particle filter can be divided in different, but connected phases. In the developed version, apart from the initial particle distribution, the algorithm is split into three phases: prediction, importance weighing, and resampling. The aim of this section is to describe the operations performed in each of these phases.

4.2.1 Initial particle distribution

Regarding the initial particle distribution, in the context of this work, only two types of distributions were used, Gaussian and uniform. If there is absolutely no knowledge of the robots initial position, the particles are uniformly distributed throughout the map and the center of the map is assumed to be the starting position. However, if there is some idea of the robot's starting position, the particles will follow a Gaussian distribution with mean μ_i and a standard deviation σ_i. The value μ_i of represents the first state estimation (the first estimation of the robot's position). The value of σ_i is the parameter that represents the uncertainty of the estimation of the starting position. Figures 4.1a and 4.1b show two Gaussian distributions of the particles, with σ_i equal to 0.6 meters and 1.2 meters, respectively.

Figure 4.2 shows 1000 particles uniformly distributed throughout the map. This is the distribution that will be used to explain the next phases of the particle filter operation. Since the ground truth position is completely unknown to the particle filter in this case, the first estimated position is considered to be the center of the map.

The fundamental effect of the selected number of particles N, is that, within a reasonable range of values, a higher number of particles will result in greater precision and faster convergence of the filter's estimation to the actual robot's position. This is due to the fact that a higher number of particles represents an higher number of states, thus increasing the probability of having a particle whose state is closer to real current state. This is especially true when the starting position is unknown and the particles are uniformly distributed throughout

the map with a large area. Still, an obvious drawback to using a higher number of particles is the need for more computational resources.

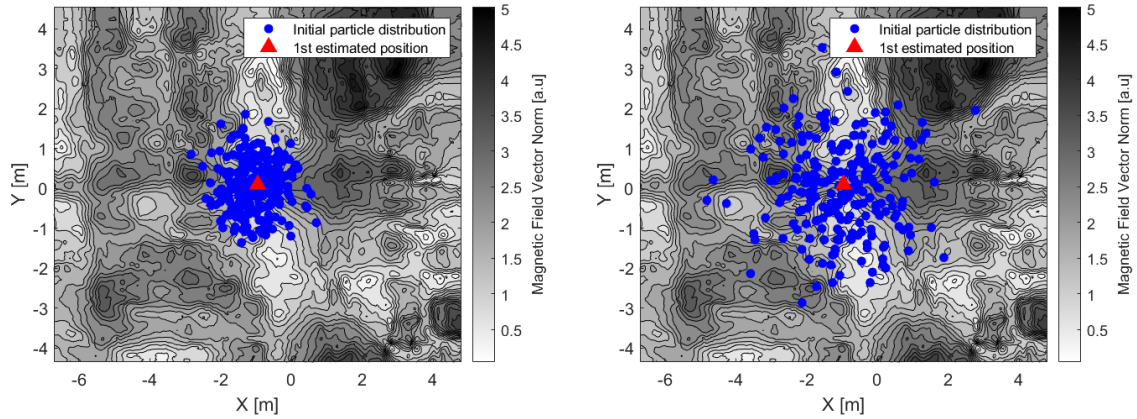

(a) $\mathcal{N}(X_0, 0.6)$ **(b)** $\mathcal{N}(X_0, 1.2)$

Figure 4.1: Initial Gaussian distributions of particles.

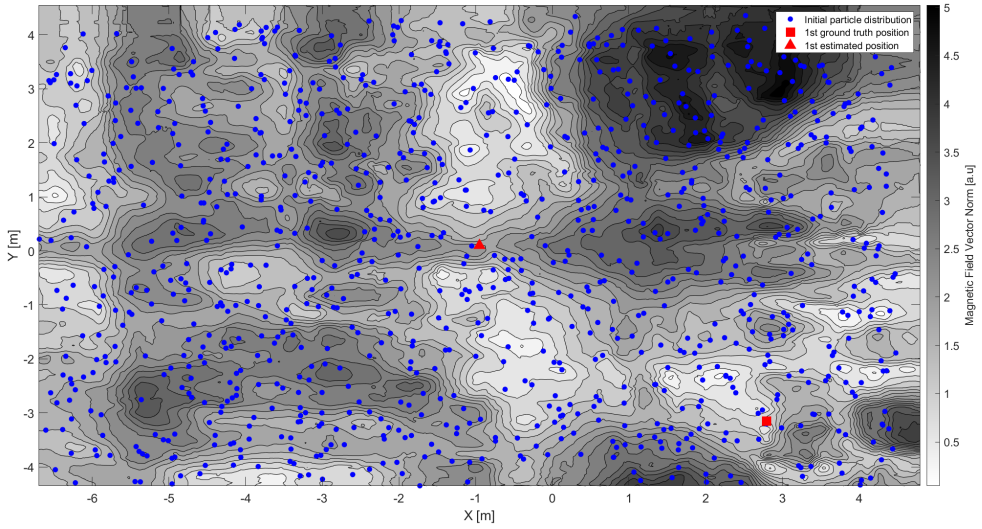

Figure 4.2: Initial uniform distribution of particles (N=1000).

4.2.2 Prediction

Following the initial particle distribution and definition of the first state, comes the prediction phase, where the next state is predicted. This prediction is based on the motion model f, the previous state X_{t-1} and the system's inputs U_t. Considering that U_t represents the processed odometry measurements that give a rough estimation of how much the robot moved since the last iteration, the motion model is defined in Equation 4.2.

$$f(X_{t-1}, U_t) = X_{t-1} + U_t \tag{4.2}$$

The odometry measurements have a significant error, which accumulates over time. To model this error and further disperse the particles, some noise W_t is intentionally added to the process model. This noise is sampled from of a Gaussian distribution with mean equal to zero and standard deviation σ_u. Evidently, the higher the value chosen for σ_u, the more the particles will be dispersed. Equation (4.3) shows how the current predicted state $\hat{X}_t$ is calculated.

$$\hat{X}_t = f(X_{t-1}, U_t) + W_t \quad \text{with} \quad W_t \sim \mathcal{N}(0, \sigma_u) \tag{4.3}$$

Figure 4.3 illustrates how the predicted state is derived from the previous state, based on the process model. Clearly, the predicted movement is different for each particle, due to the added noise W_t.

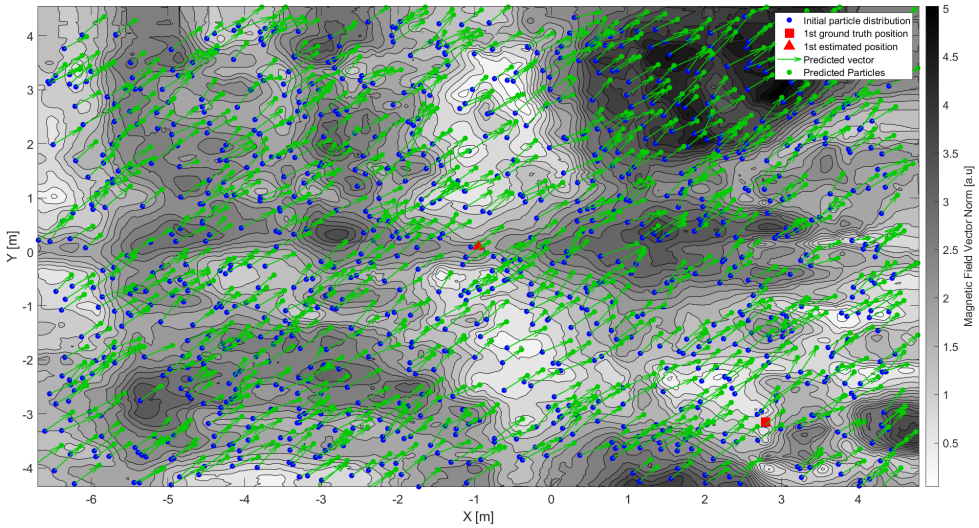

Figure 4.3: Prediction of current state, based on the previous state and the motion model.

Next, the predicted measurements $\hat{Z}_t$ are calculated. The predicted measurements are computed as a function of the predicted state $\hat{X}_t$, as defined by the measurement model g. Equation (4.4) shows how the predicted measurements are calculated. In the context of this work, the predicted measurements represent the magnetic field vector norm at the predicted position of each particle.

$$\hat{Z}_t = g(\hat{X}_t) \tag{4.4}$$

4.2.3 Importance weighing

In this phase, the predicted measurements $\hat{Z}_t$ are compared with the current measurement acquired by the magnetometer Z_t. As a result of this comparison, each particle is given a weight $w_t^{[i]}$, based on the likelihood of measuring Z_t, given the current state $X_t{}^{[i]}$. This

likelihood is presented in Equation (4.5) and is modeled by the Gaussian distribution (with standard deviation σ_z) used in Equation (4.1) to model the measurement error V_t.

$$p(Z_t|\hat{X}_t^{[i]}) = \frac{1}{\sigma_z\sqrt{2\pi}} e^{-\frac{1}{2}\left(\frac{Z_t - \hat{Z}_t^{[i]}}{\sigma_z}\right)^2} \tag{4.5}$$

Moreover, the weights are updated recursively and depend on the weights of the previous state. Equation (4.6) shows how the weight of each particle is calculated.

$$w_t^{[i]} = w_t^{[i-1]} p(Z_t|\hat{X}_t^{[i]}) \tag{4.6}$$

In terms of the particle filter operation, the value of σ_z defines how sensitive the calculated particle weights are to the difference between the current measurement taken by the magnetometer Z_t and the predicted magnetic field vector norm at the particle's location $\hat{Z}_t^{[i]}$. A higher σ_z would result in a higher calculated particle weight, and vice-versa.

Furthermore, a higher weight is given to particles that register a predicted measurement $\hat{Z}_t^{[i]}$ whose value is closer to the current measurement acquired by the magnetometer Z_t. On the other hand, if the predicted measurement for a given particle has a value that is significantly different from the measurement taken by the magnetometer, that particle is given a lower weight. Essentially, the higher the weight of a particle, the more influence it will have on estimating robot's position.

Figure 4.4 shows the weighted particles. It is clear that the particles in the darker areas of the map, which represent a stronger magnetic field, have lower weights. This was expected, since the ground truth position, where the current measurement was acquired, is in a lighter area of the map, which represents a weaker magnetic filed. Hence, in the darker regions, the matching between the predicted and the real measurements is poorer, resulting in lower particle weights.

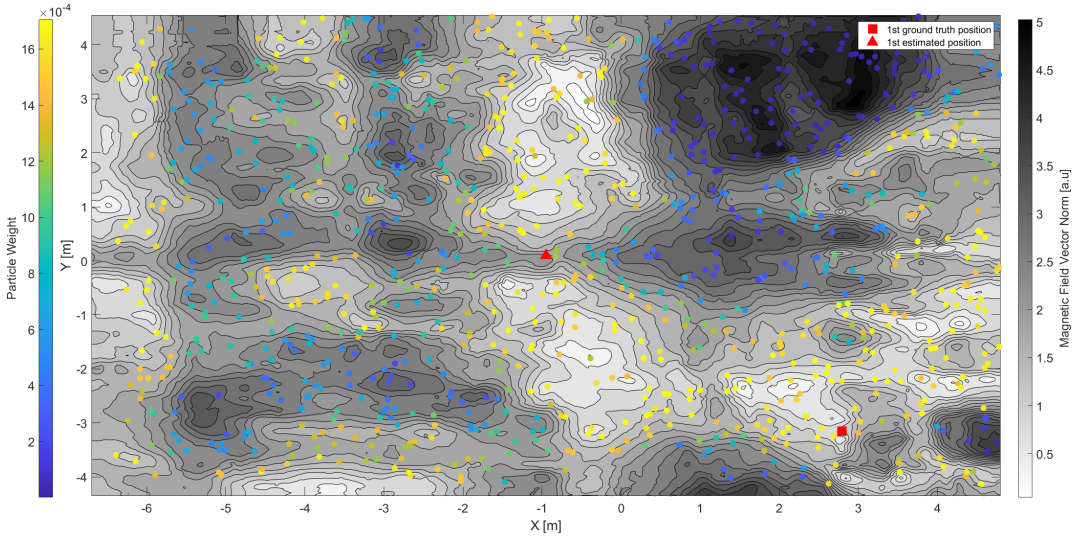

Figure 4.4: Weighted particles after the importance sampling phase.

4.2.4 State Estimation

In the context of this work, the state estimate $\bar{X}_t$, represents the current estimate of the robot's position. First, all the particle weights should be normalized, so that Equation (4.7) is verified and the sum of all weights is equal to 1. One approach to calculating the state estimate is to perform a weighed average of all the particle states, based on the particle weights, as is defined in Equation (4.8). This way, the state of each particle is multiplied by the respective weight and the particles with higher weights will have more influence in determining the current state estimate.

$$\sum_{i=1}^{N} w_t^{[i]} = 1 \tag{4.7}$$

$$\bar{X}_t = \frac{1}{N} \sum_{i=1}^{N} w_t^{[i]} X_t^{[i]} \tag{4.8}$$

4.2.5 Resampling

An additional action, that may not be performed in every iteration, but is essential nonetheless, is the resampling. When the resampling is applied, the particles with lower weights are substituted by the particles with higher weights.

While there are various versions on when and how to perform the resampling, the selected method relies on a metric named effective number of particles N_{eff}, calculated through Equation (4.9) [20] [21].

$$N_{eff} = \frac{1}{\sum_{i=1}^{N} (w_t^{[i]})^2} \tag{4.9}$$

The effective number of particles is used to define the resampling rate because it reflects the disparity between the particle weights. If all particles have the same weight, the effective number of particles will be equal to the total number of particles. On the other hand, if few particles have a high weight and most particles have a low weight, the effective number of particles will be lower than the total number of particles. Thus, when the ratio between the effective number of particles N_{eff} and the number of particles N drops bellow the value of a a parameterizable threshold T_{eff}, the particles are resampled.

Algorithm 1 presents a section of pseudo-code that describes the resampling algorithm. The first line contains the resampling condition. On Line 3, a random namber is sampled from a uniform distribution between 0 and 1. The j index calculated on Line 5, represents which particle will substitute the current particle with index i. It should be noted that, while it is likely that the particle with index j will have a high weight, this is not guaranteed. This is justified by the fact that the particles with lower weights also have some probability of representing the current position of the robot.

Algorithm 1 Resampling algorithm

1: **if** $\frac{N_{eff}}{N} \leq T_{eff}$ **then**
2: **for** each i particle **do**
3: Sample $rand$ from $\mathcal{U}(0, 1)$
4: w_{cs} = cumulative sum of w_t
5: j = lowest index of w_{cs} that satisfies $w_{cs}^{[j]} \geq rand$
6: $X_t^{[i]} = X_t^{[j]}$
7: $w_t^{[i]} = w_t^{[j]}$
8: **end for**
9: **end if**

Figure 4.5 shows the weighted resampled particles. When comparing this distribution with the distribution shown in Figure 4.4, it can be observed that some of the particles with lower weights have been moved to location of the particles with higher weights. It is also important to note that the total number of particles remains exactly the same, but some of the particles share the same position after the resampling is performed and become superimposed.

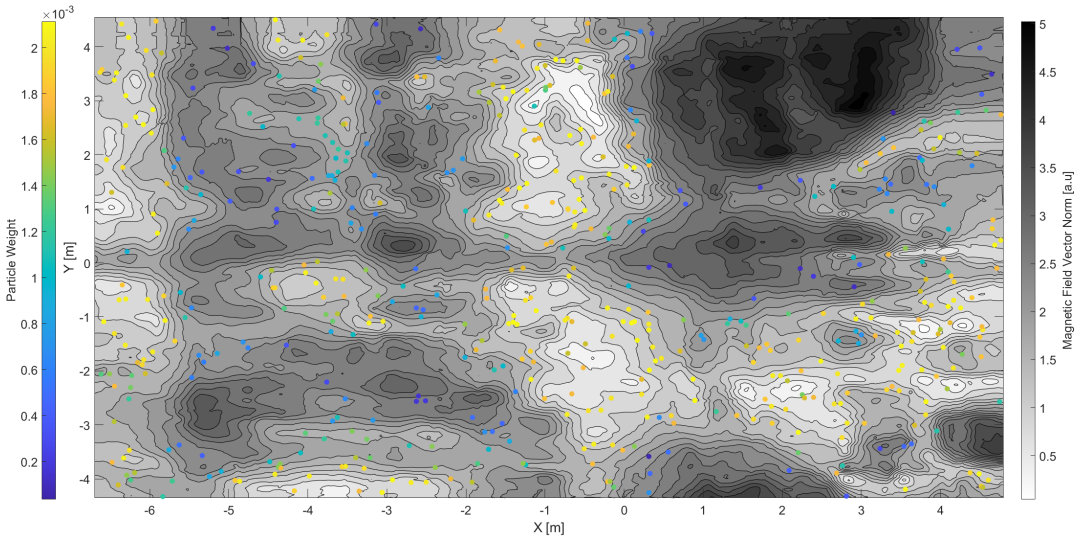

Figure 4.5: Particle distribution after performing the resampling.

4.2.6 Implemented algorithm

Algorithm 2 presents the localization algorithm, with all the operations described in this chapter. Lines 1 through 4 represent the initial particle distribution (for the case where the particles follow a Gaussian distribution). The d_m parameter (Line 7) refers to the minimum distance (given by the odometry measurements) that the robot must travel since the last iteration, in order to enter a new iteration, update the particles and calculate the next state estimate. Lines 9 and 10 refer to the prediction phase. The importance weighing and state estimation are performed in Lines 11 and 13, respectively. Lines 16 through 24 correspond to the resampling algorithm previously presented.

Algorithm 2 Localization Algorithm

for each i particle **do**
    Sample $X_0^{[i]}$ from $\mathcal{N}(\mu_i, \sigma_i)$
    $w_0^{[i]} = \frac{1}{N}$
end for
$\bar{X}_0 = \frac{1}{N} \sum_{i=1}^{N} w_0^{[i]} X_0^{[i]}$
while robot is moving **do**
    if $\|U_t\| \geq d_m$ **then**
        for each i particle **do**
            $\hat{X}_t^{[i]} = X_{t-1}^{[i]} + U_t + \mathcal{N}(0, \sigma_u)$
            $\hat{Z}_t^{[i]} = g(\hat{X}_t^{[i]})$
            $w_t^{[i]} = w_t^{[i-1]} p(Z_t | \hat{X}_t^{[i]})$
            $X_t^{[i]} = \hat{X}_t^{[i]}$
            $\bar{X}_t = \frac{1}{N} \sum_{i=1}^{N} w_t^{[i]} X_t^{[i]}$
        end for
        $N_{eff} = \frac{1}{\sum_{i=1}^{N} (w_t^{[i]})^2}$
        if $\frac{N_{eff}}{N} \leq T_{eff}$ **then**
            for each i particle **do**
                Sample $rand$ from $\mathcal{U}(0, 1)$
                w_{cs} = cumulative sum of w_t
                j = lowest index of w_{cs} that satisfies $w_{cs}^{[j]} \geq rand$
                $X_t^{[i]} = X_t^{[j]}$
                $w_t^{[i]} = w_t^{[j]}$
            end for
        end if
    end if
end while

CHAPTER 5

Experiments and Results

The aim of this chapter is to present and discuss the results of the tests performed to validate the localization algorithm presented in Chapter 4. On all tests, the robot was remotely controlled and made to perform an arbitrary trajectory on the mapped environment presented in Chapter 3, while acquiring the magnetic field data, the ground truth position and odometry measurements.

A version of the particle filter was implemented in MATLAB R2019b. First, the acquisition was performed. Subsequently, the acquired odometry and magnetometer measurements were supplied to the filter, which tried to continuously estimate the robot's position. In order to assess the performance of the filter, the position estimated by the particle filter was compared with the ground truth position. Finally, a thorough assessment of the filters accuracy and robustness was performed in a series of Monte Carlo simulations consisting of 1000 runs of each navigation experiment.

Table 5.1 presents the values selected for some parameters used in all the experiments, using the same notation defined in Table 4.1 and described in Chapter 4. On all the figures presented in this chapter, the squares mark the starting position and the asterisks mark the final position.

Parameter	**Value**
N	2000
d_m	0.1 m
σ_u	0.06 m
σ_z	0.25 a.u.
T_{eff}	0.75

Table 5.1: Value of parameters used throughout all the experiments.

5.1 Test with a known starting position and no initial positioning error.

On the first test, the particle filter was supplied with the starting ground truth position. The aim of this test was to verify that the particle filter could correct the expected cumulative

error given by the odometry measurements. Figure 5.1 shows the ground truth position with a contour map of the ambient magnetic field vector norm on the background.

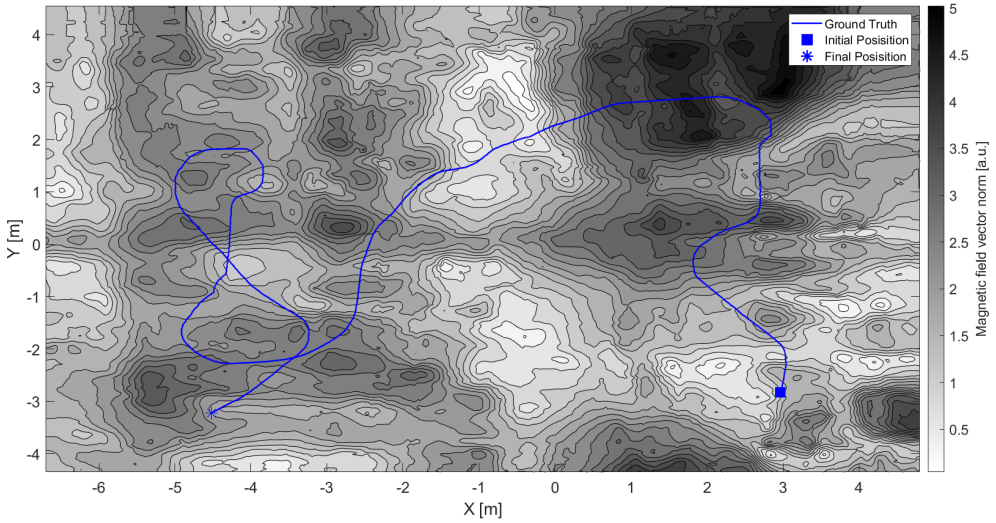

Figure 5.1: Ground truth trajectory of test with a known starting position and no initial positioning error, with the magnetic contour map in the background.

Figure 5.2 shows the ground truth position, the position given only by the processed odometry measurements and the position estimated by the particle filter. As the robot travels more distance, the position given by the odometry gradually drifts from the ground-truth position. Clearly, the particle filter was able to successfully correct the cumulative error given by the odometry.

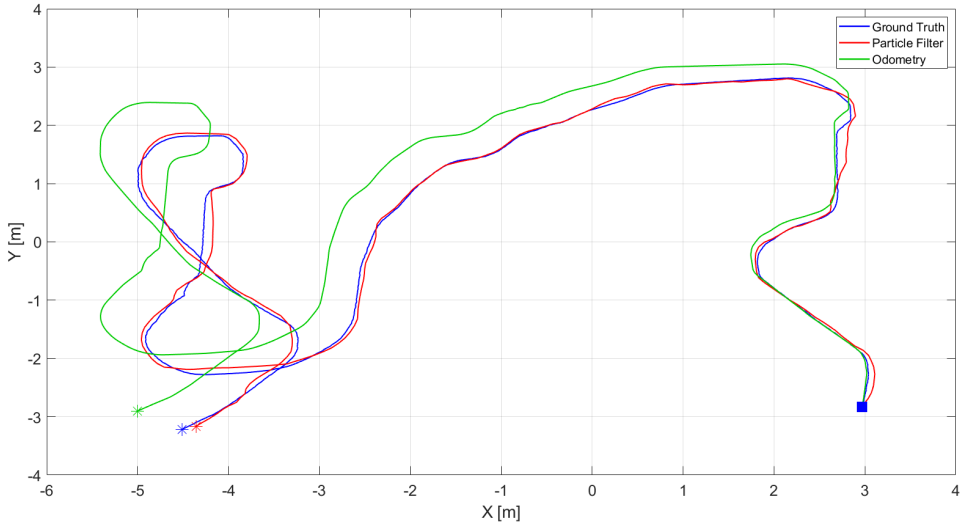

Figure 5.2: Ground truth, odometry and particle filter estimated trajectories of test with a known starting position and no initial positioning error.

Figure 5.3 shows the evolution of the particle distribution throughout the experiment.

Since the range of the particle weight values is different in every iteration and the purpose is to roughly illustrate the evolution of the particles distribution, the color associated to each particle weight is not presented. Nevertheless, the particles with a lighter colour (yellow) have higher weights and the particles with a darker colour (blue) have lower weights. The same applies for Figures 5.6, 5.10 and 5.14, presented in the following sections. Initially, the particles followed a normal distribution, with a mean (μi) equal to the initial ground truth position and a standard deviation (σ_i) of 0.3 meters. The particles remained in the vicinity of the ground truth position throughout the entirety of the experiment.

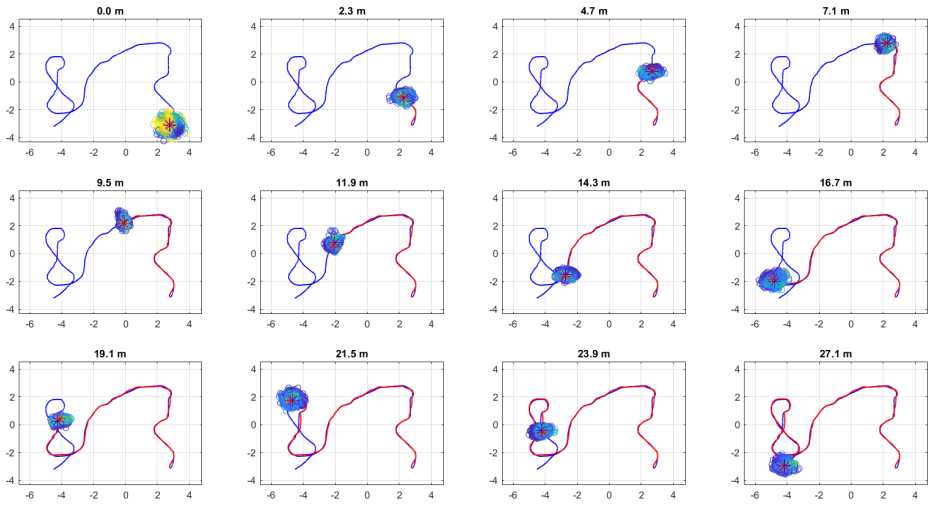

Figure 5.3: Evolution of particle distribution of test with a known starting position and no initial positioning error. The lighter colours indicate higher particles weights and the title of each sub-figure indicates the distance travelled by the robot.

Figure 5.4 shows how the distance error of the both the odometry and particle filter estimated positions evolves as the robot performs the trajectory. Every time the processed odometry measurements indicated that the robot had moved an additional 0.1 meters, the particle filter positioning error was determined by calculating the distance between the position estimated by the particle filter at that time and the ground truth position. The same was done to calculate the odometry positioning error. As expected, the odometry error grows steadily, reaching approximately 0.7 meters in the experiment, while the maximum registered particle filter error was 0.165 meters. Table 5.2 summarizes the results of the experiment.

Result description	**Value**
Mean of particle filter error	0.057 m
Maximum of particle filter error	0.165 m
Mean of odometry error	0.438 m
Maximum of odometry error	0.708 m

Table 5.2: Results of test with a known starting position and no initial positioning error.

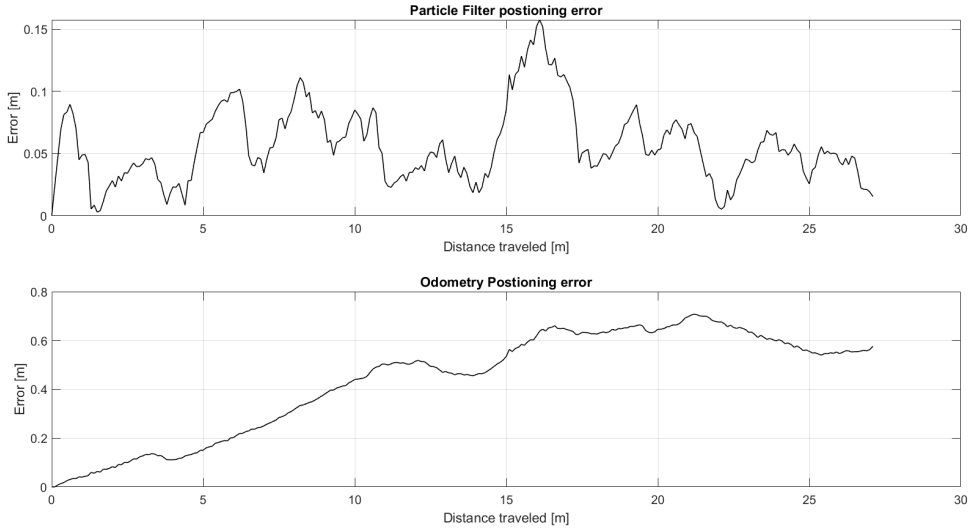

Figure 5.4: Evolution of positioning errors of test with a known starting position and no initial positioning error.

5.2 Tests with an unknown starting position and uniformly distributed particles

After demonstrating that the particle filter could correct the odometry error, the following experiments aimed at determining if the filter could converge to the ground truth position, without being supplied with it. For this purpose, the particles were uniformly distributed throughout the map and the center of the map was assumed to be the starting position.

5.2.1 First Trajectory

On the first experiment, the same trajectory already presented in Figure 5.1 was considered. Figure 5.5 shows the ground truth position, the position given only by the processed odometry measurements and the position estimated by the particle filter. The filter's estimation was able to converge to a position close to the ground truth. As expected under these circumstances, the position given only by the odometry measurements presents significant error and is even temporally off the map's limits.

Figure 5.6 shows the evolution of the particle distribution throughout the robot's trajectory. As the position estimated by the particle filter converged, the particles became less dispersed and converged to an area near the ground truth position.

Figure 5.7 shows the evolution of the particle filter positioning error, which was calculated in the same way as the one described in Section 5.1 (Figure 5.4). After the robot had travelled 3.8 meters the position given by the particle filter had already converged. The point of convergence was determined as the first point where the particle filter error dropped below 0.1 meters (the same criterion was employed in Sections 5.2.2 and 5.2.3). The mean and maximum of the registered post convergence error was 0.060 meters and 0.142 meters, respectively.

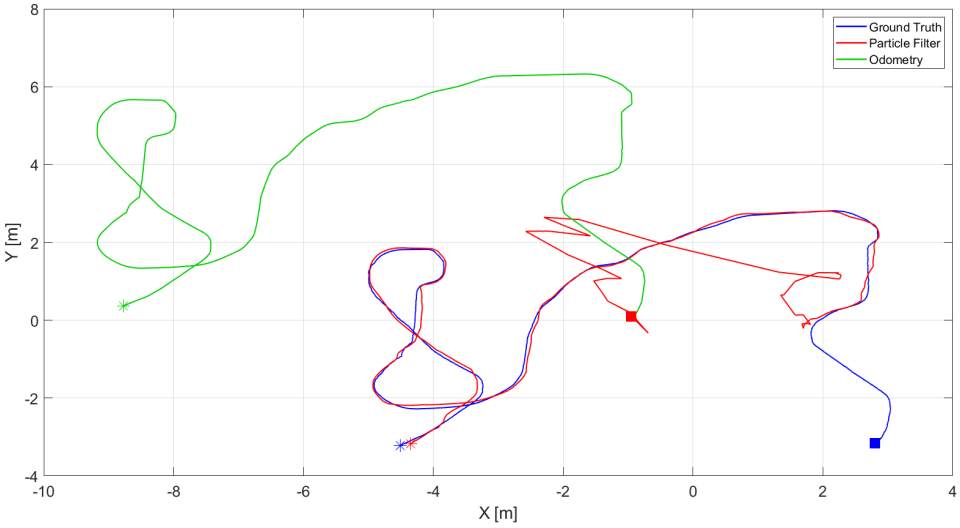

Figure 5.5: Ground truth, odometry and particle filter estimated trajectories of first test with an unknown starting position and uniformly distributed particles.

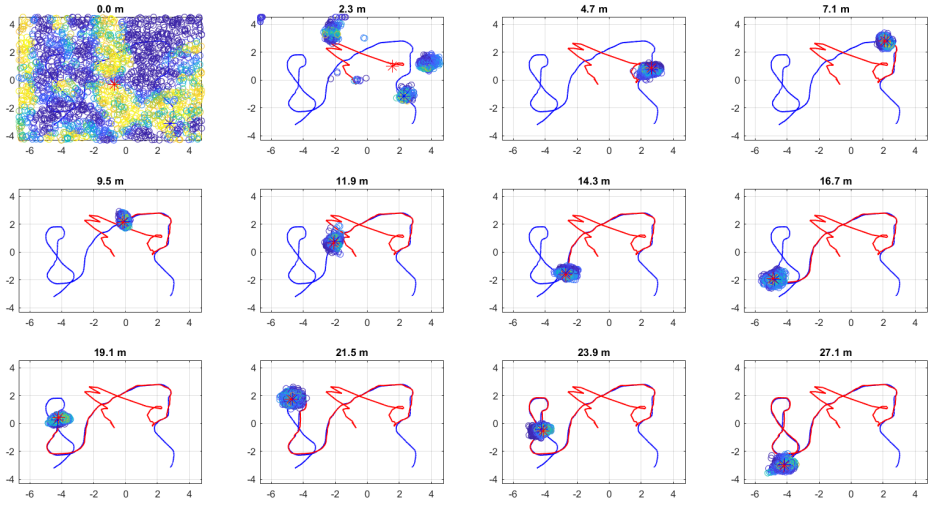

Figure 5.6: Evolution of particle distribution of first test with an unknown starting position and uniformly distributed particles. The lighter colours indicate higher particles weights and the title of each sub-figure indicates the distance travelled by the robot.

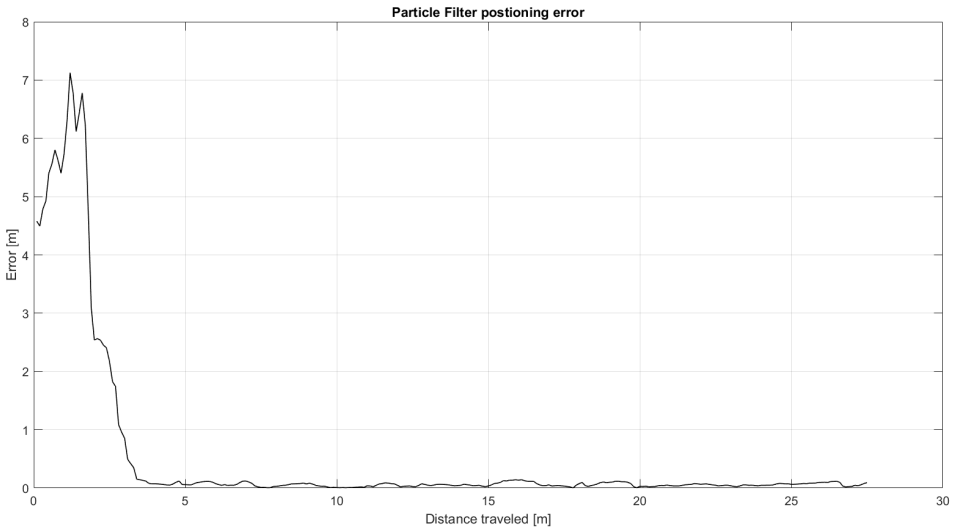

Figure 5.7: Position estimation error of first test with an unknown starting position and uniformly distributed particles.

5.2.2 Second Trajectory

The trajectory of the second experiment is presented in Figure 5.8. Figure 5.9 shows the ground truth position, the position given only by the processed odometry measurements and the position estimated by the particle filter. As was the case in the last experiment, the filter's estimation was able to converge to a position close to the ground truth.

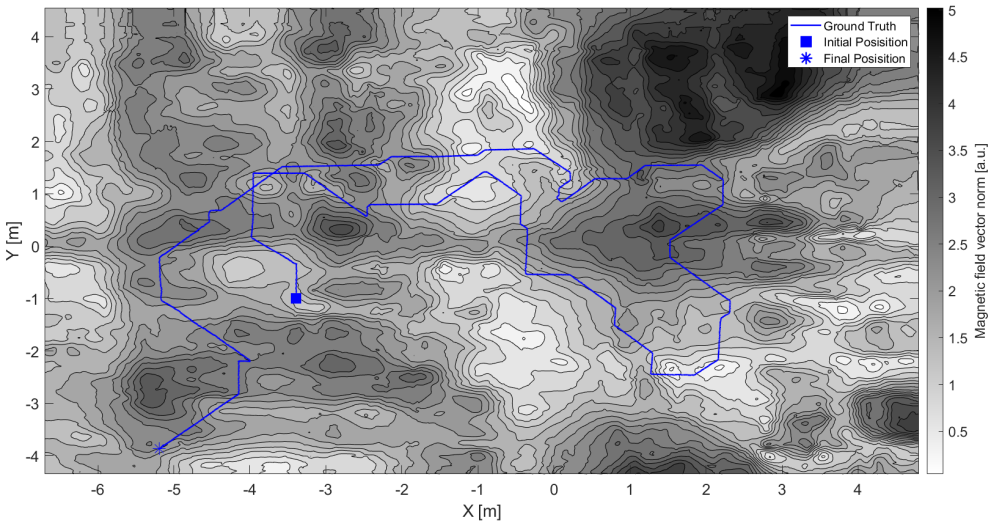

Figure 5.8: Ground truth trajectory of second test with an unknown starting position and uniformly distributed particles, with magnetic contour map in the background.

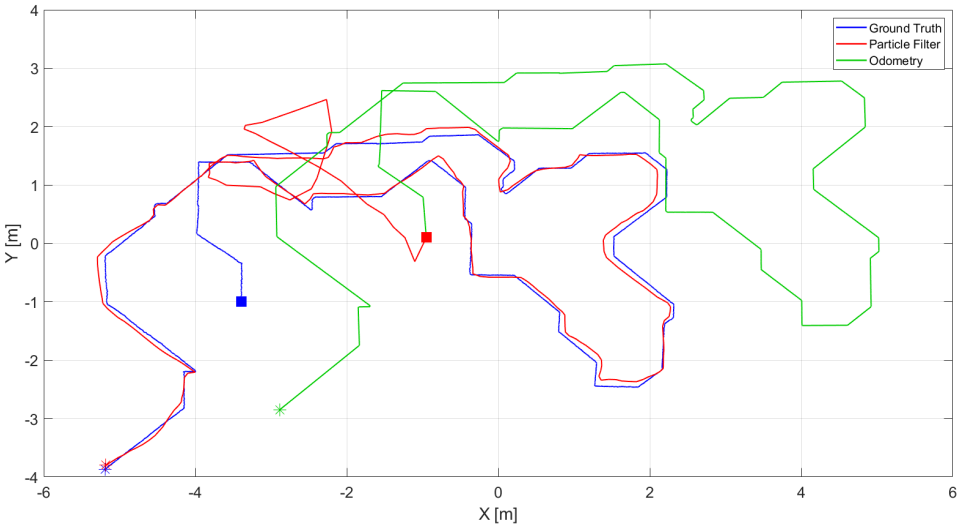

Figure 5.9: Ground truth, odometry and particle filter estimated trajectories of second test with an unknown starting position and uniformly distributed particles.

Figure 5.10 shows the evolution of the particle distribution throughout the robot's trajectory. The particles became less dispersed and converged to an area near the ground truth position.

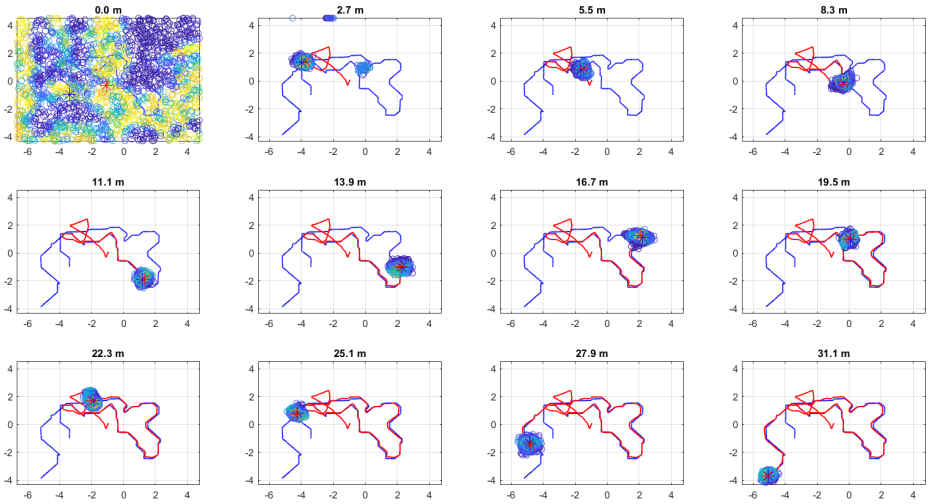

Figure 5.10: Evolution of particle distribution of second test with an unknown starting position and uniformly distributed particles.The lighter colours indicate higher particles weights and the title of each sub-figure indicates the distance travelled by the robot.

Figure 5.11 shows the evolution of the particle filter positioning error. The filter's estimation converged to the ground position after the robot had travelled 3.2 meters. The mean and maximum of the registered post convergence error was 0.079 meters and 0.168 meters, respectively.

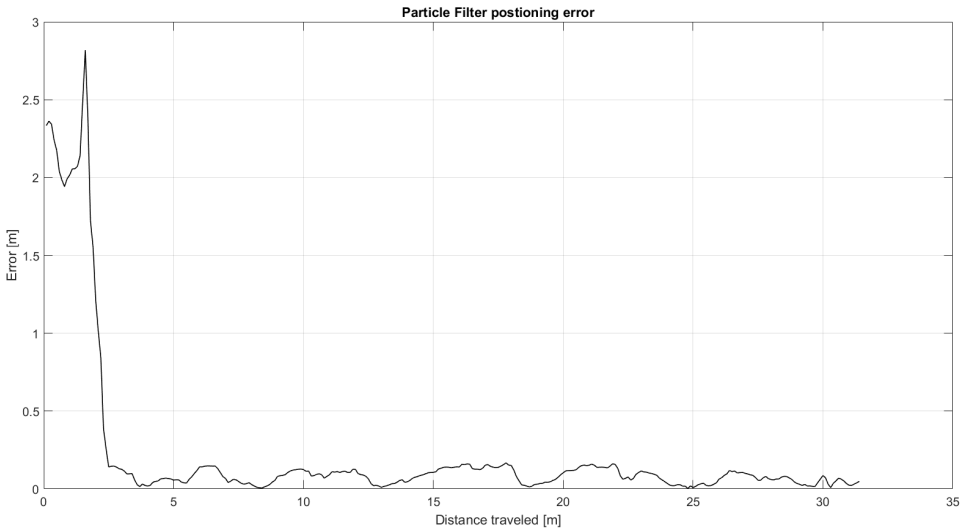

Figure 5.11: Position estimation error of second test with an unknown starting position and uniformly distributed particles.

5.2.3 Third Trajectory

The trajectory of the third experiment is presented in Figure 5.12. Figure 5.13 shows the ground truth position, the position given only by the processed odometry measurements

and the position estimated by the particle filter. Again, the filter's estimation successfully converged to a position close to the ground truth.

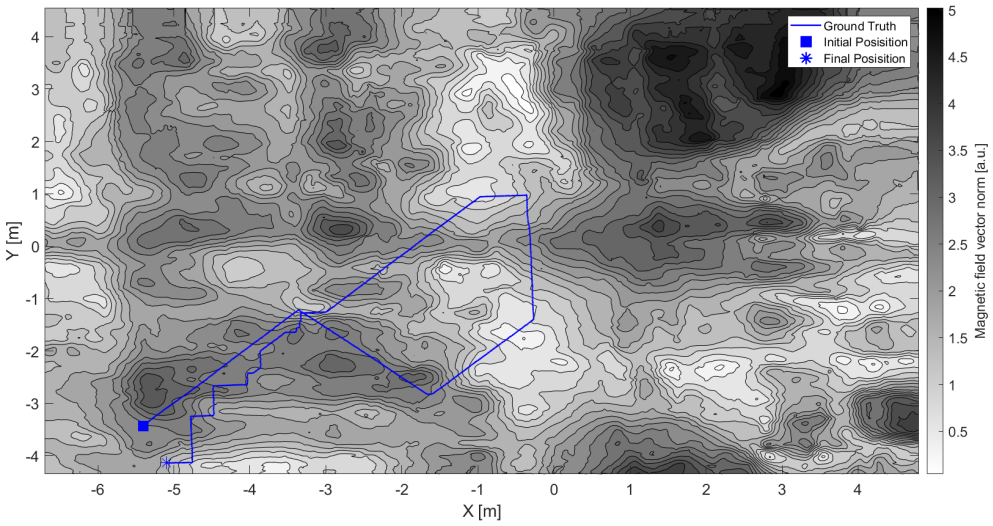

Figure 5.12: Ground truth trajectory of third test with an unknown starting position and uniformly distributed particles, with magnetic contour map in the background.

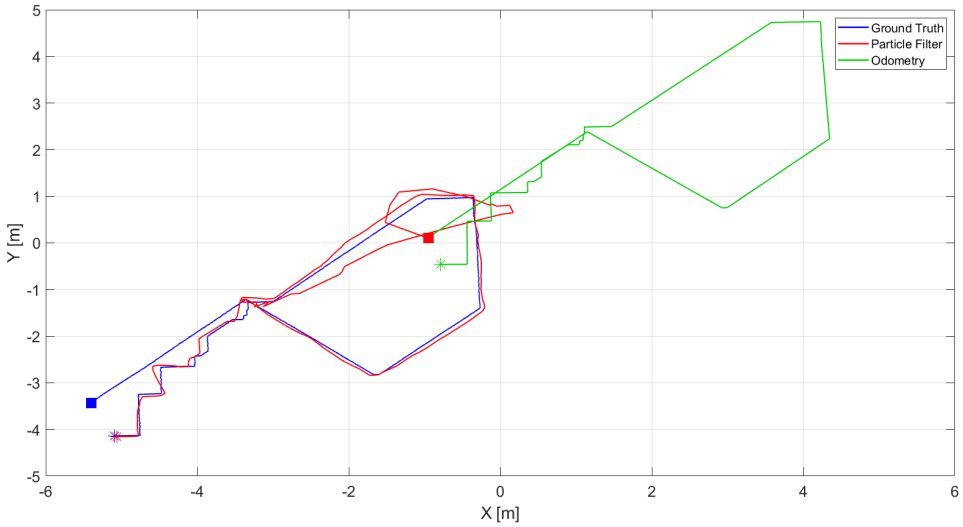

Figure 5.13: Ground truth, odometry and particle filter estimated trajectories of third test with an unknown starting position and uniformly distributed particles.

Figure 5.14 shows the evolution of the particle distribution throughout the robot's trajectory. As was the case in the last two experiments, the particles became less dispersed and converged to an area near the ground truth position.

Figure 5.15 shows the evolution of the particle filter positioning error. The filter's estimation converged to the ground position after the robot had travelled 3.1 meters. The mean and maximum of the registered post convergence error was 0.075 meters and 0.172

meters, respectively.

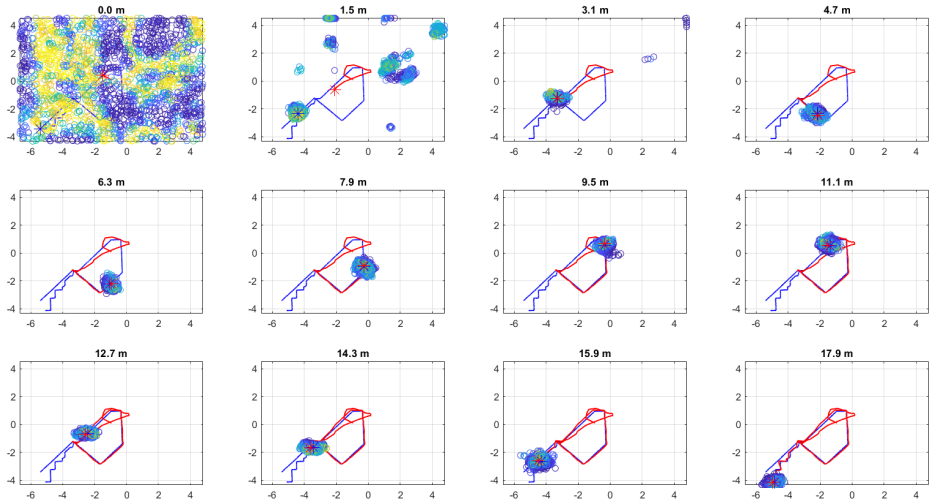

Figure 5.14: Evolution of particle distribution of third test with an unknown starting position and uniformly distributed particles. The lighter colours indicate higher particles weights and the title of each sub-figure indicates the distance travelled by the robot.

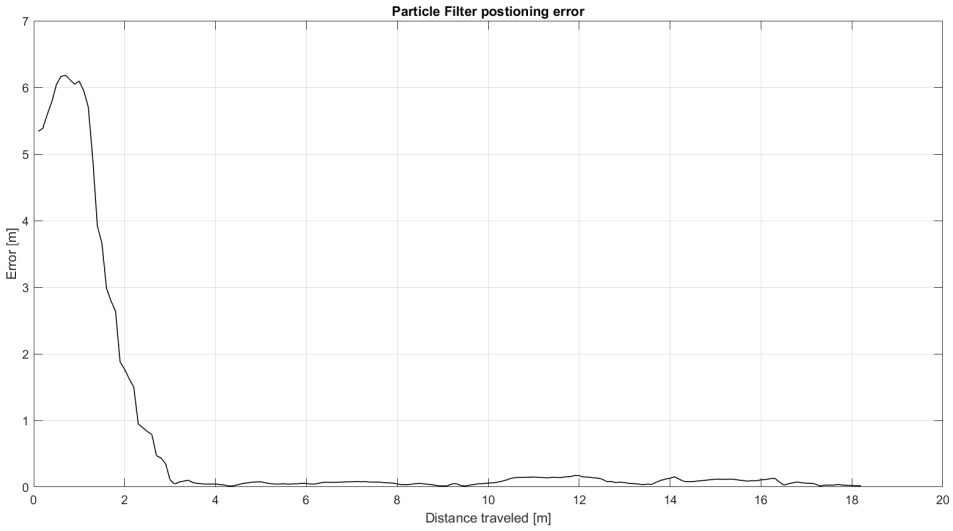

Figure 5.15: Position estimation error of third test with an unknown starting position and uniformly distributed particles.

Table 5.3 summarizes the results of all the experiments with an unknown starting position and uniformly distributed particles.

Result description	Value
Convergence distance for the first trajectory	3.8 m
Mean of post convergence particle filter error for the first trajectory	0.060 m
Maximum of post convergence particle filter error for the first trajectory	0.142 m
Convergence distance for the second trajectory	3.2 m
Mean of post convergence particle filter error for the second trajectory	0.079 m
Maximum of post convergence particle filter error for the second trajectory	0.168 m
Convergence distance for the third trajectory	3.1 m
Mean of post convergence particle filter error for the third trajectory	0.075 m
Maximum of post convergence particle filter error for the third trajectory	0.172 m

Table 5.3: Results of tests with an unknown starting position and uniformly distributed particles.

5.3 Monte Carlo Experiments

In order to test the robustness of the algorithm, four Monte Carlo experiments were performed, using the same measurement data presented in the previous sections. The same value was attributed to each of the parameters presented in Table 5.1. For each experiment, an initial new set of particles was randomly generated, following either a Gaussian or uniform distribution. Likewise, new motion and measurement model error distributions were generated on every iteration (with the same standard deviations σ_u and σ_z, respectively).

5.3.1 First Trajectory with a known starting position and no initial positioning error

In this experiment, 1000 simulations were performed with the same trajectory and starting position considered in Section 5.1. A new initial particle distribution was generated for each simulation, which followed a gaussian distribution with a mean μ_i equal to the starting position and a standard deviation σ_i of 0.3 meters.

Figure 5.16 shows the evolution of the particle filter estimation error for all simulations and Table 5.4 summarizes the results of the experiment. The results were similar in all simulations and confirm that the particle filter was able to consistently correct the odometry error.

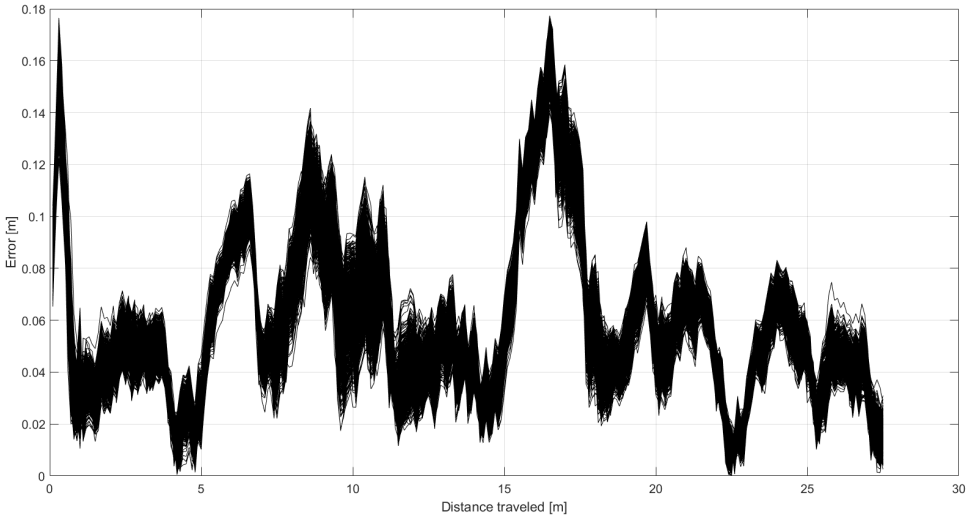

Figure 5.16: Evolution of particle filter estimation error for 1000 simulations of test with a known starting position and no initial positioning error.

Result description	Value
Mean of particle filter error	0.069 m
Maximum of particle filter error	0.179 m

Table 5.4: Results of Monte Carlo experiment with a known starting position and no initial positioning error.

5.3.2 Trajectories with an unknown starting position and uniformly distributed particles

Next, three Monte Carlo experiments were performed, each consisting of 1000 simulations, with each of the three trajectories previously presented. Figures 5.17, 5.18 and 5.19 present the evolution of the particle filter estimation error for all simulations with the same trajectories and starting positions considered in Sections 5.2.1, 5.2.2 and 5.2.3, respectively. A new initial particle distribution was generated for each simulation, which a followed an uniform distribution.

Out of all 3000 simulations of all experiments, the particle filter estimation successfully converged to the ground truth position in 2998 simulations. Regardless, on some simulations the distance travelled by the robot needed for the particle filter estimation to converge was higher than the one registered in the experiments presented in Section 5.2. On each Monte Carlo experiment, after convergence, the behaviour of the error function was similar on all simulations.

Table 5.5 summarizes the results for all the Monte Carlo experiments with an unknown starting position and uniformly distributed particles.

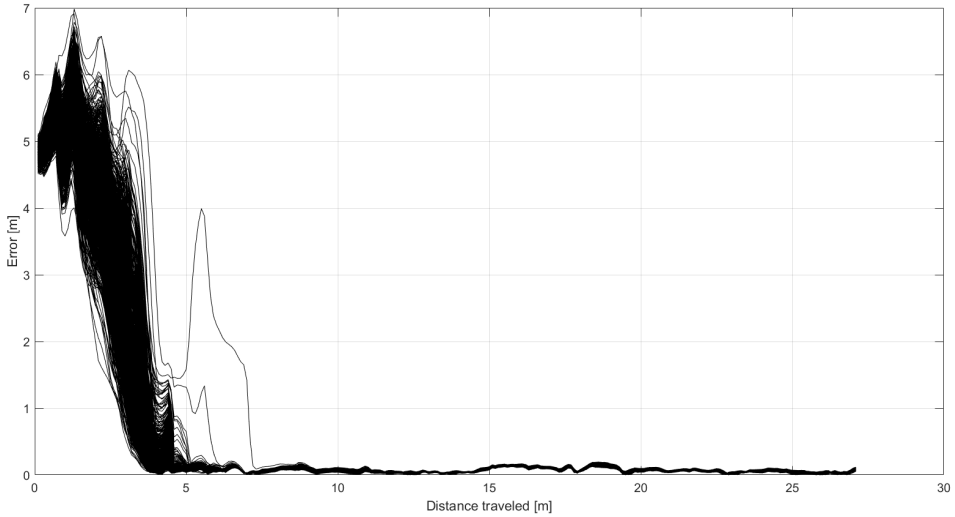

Figure 5.17: Evolution of particle filter estimation error for 1000 simulations of the first trajectory with an unknown starting position and uniformly distributed particles.

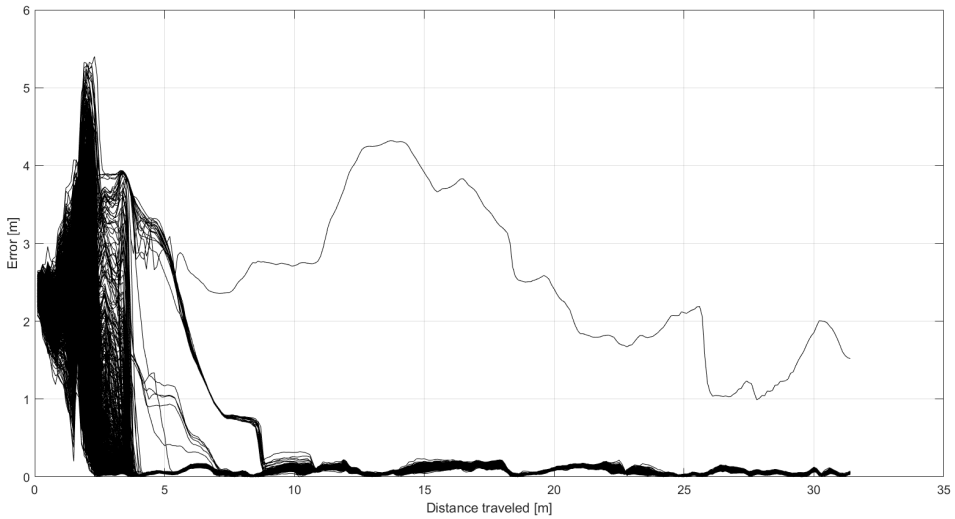

Figure 5.18: Evolution of the particle filter estimation error for 1000 simulations of second trajectory with an unknown starting position and uniformly distributed particles.

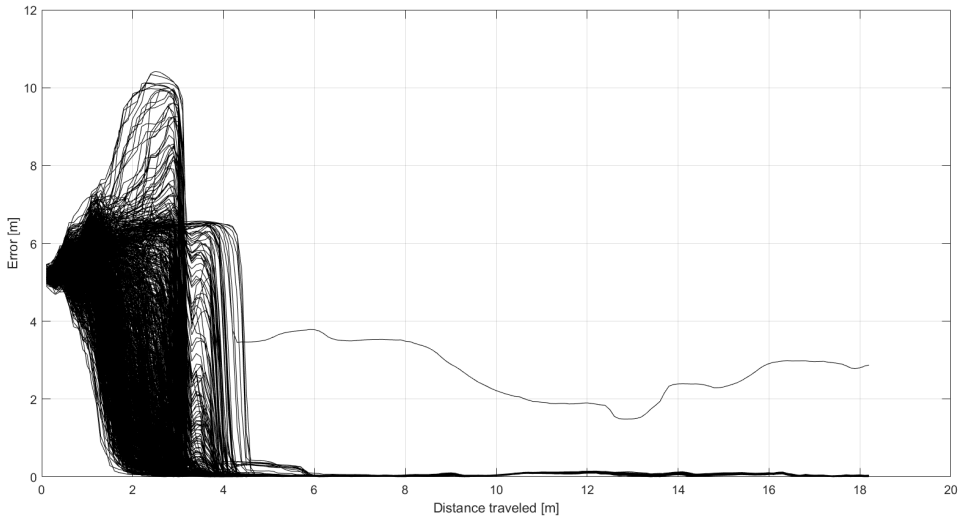

Figure 5.19: Evolution of the particle filter estimation error for 1000 simulations of third trajectory with an unknown starting position and uniformly distributed particles.

Result description	**Value**
Number of converging simulations for the first trajectory	1000 out of 1000
Mean of post convergence particle filter error for the first trajectory	0.068 m
Maximum of post convergence particle filter error for the first trajectory	0.196 m
Number of converging simulations for the second trajectory	999 out of 1000
Mean of post convergence particle filter error for the second trajectory	0.083 m
Maximum of post convergence particle filter error for the second trajectory	0.209 m
Number of converging simulations for the third trajectory	999 out of 1000
Mean of post convergence particle filter error for the third trajectory	0.070 m
Maximum of post convergence particle filter error for the third trajectory	0.188 m

Table 5.5: Results of Monte Carlo experiments with an unknown starting position and uniformly distributed particles.

CHAPTER 6

Summary and conclusions

There are a variety of positioning techniques, each with its advantages and disadvantages. There is not one single solution for every case. Each situation is different, has its own requirements and there is usually a trade-off between accuracy, reliability, complexity, price and other attributes.

The work presented in this dissertation, explores a solution that, while there already exists some recent research on, is yet to be popularized and implemented to its full potential. Ambient magnetic field based systems can be very accurate, power efficient, implemented with low cost hardware and mitigate the privacy issues of other positioning technologies. On the other hand, they may be unreliable, as they are dependant on the magnetic features of the environment.

The process followed to create and validate the magnetic map was characterized, since a good magnetic map is as important as an accurate localization algorithm. The adopted interpolation method used to create the magnetic map was ordinary Kriging, which is broadly used in a geostatistical context. This method often yields accurate results, even when the mapping acquisition is not considerably dense.

The performed experiments indicate that the developed localization algorithm is reliable and accurate enough to address many indoor localization problems. Out of all experiments where the filter's estimation was able to converge to the ground truth position, a mean positioning error of less than 10 centimeters was registered (after the particle filter had converged). Moreover, regarding the experiments where the algorithm was not supplied with the robot's initial position, the filter was able to successfully converge to the ground truth position on 2998 out of 3000 simulations.

In conclusion, the results are encouraging and demonstrate that it is possible to achieve a localization accurate enough to solve many mobile robot navigation problems using magnetic data. Nevertheless, there needs to be more work done in order to further test the reliability of these types of systems. This implies performing more tests in different environments and under diverse conditions.

6.1 Future Work

One of the more obvious possibilities that was not explored in the work presented in this dissertation, is the use of the full magnetic field vector instead of just the vector norm. This would imply taking into account the robot's orientation, but would also provide a lot more information that could improve the accuracy of the localization algorithm.

The magnetometer used to measure the ambient magnetic field, is more expensive and accurate than the more mainstream MEMS-based sensors present in everyday devices, such as mobile phones. Another interesting possibility would be to install one of these less costly magnetometers on the robot and evaluate the impact on the results. Moreover, more than one magnetometer could be placed on the robot, which would enable the estimation of the robot's orientation and possibly increase the accuracy of the estimated position.

References

[1] W. Sakpere, M. Adeyeye Oshin, and N. Mlitwa, "A state-of-the-art survey of indoor positioning and navigation systems and technologies", *South African Computer Journal*, vol. 29, p. 145, Dec. 2017. DOI: 10.18489/sacj.v29i3.452.

[2] Z. Farid, R. Nordin, and M. Ismail, "Recent advances in wireless indoor localization techniques and system", *Journal of Computer Networks and Communications*, vol. 2013, Sep. 2013. DOI: 10.1155/2013/185138.

[3] F. Zafari, A. Gkelias, and K. K. Leung, "A survey of indoor localization systems and technologies", *IEEE Communications Surveys Tutorials*, vol. 21, no. 3, pp. 2568–2599, 2019. DOI: 10.1109/COMST.2019.2911558.

[4] Mai A. Al-Ammar, Suheer Alhadhrami, AbdulMalik Al-Salman Abdulrahman Alarifi, Hend S. Al-Khalifa, Ahmad Alnafessah, Mansour Alsaleh, "Comparative Survey of Indoor Positioning Technologies, Techniques, and Algorithms", 2014.

[5] M. J. Mataric, *The Robotics Primer*. The MIT Press, 2007.

[6] H. F. D.-W. John J. Leonard, *Directed Sonar Sensing for Mobile Robot Navigation*. Springer, 1992.

[7] J. Haverinen and A. Kemppainen, "Global indoor self-localization based on the ambient magnetic field", *Robotics and Autonomous Systems*, vol. 57, pp. 1028–1035, Oct. 2009. DOI: 10.1016/j.robot.2009.07.018.

[8] M. Frassl, M. Angermann, M. Lichtenstern, P. Robertson, B. J. Julian, and M. Doniec, "Magnetic maps of indoor environments for precise localization of legged and non-legged locomotion", pp. 913–920, 2013. DOI: 10.1109/IROS.2013.6696459.

[9] D. K. Cheng, *Field and Wave Electromagnetics Second Edition*. Tsinghua University Press, 1989.

[10] J. D. Jackson, *Classical Electrodynamics Third Editon*. John Wiley & Sons Inc, 1998.

[11] R. J. Blakely, *Potential Theory in Gravity and Magnetic Applications*. Cambridge University Press, 1996.

[12] J. W. J. J. Raymond A. Serway, *Physics for Scientists and Engineers with Modern Physics Ninth Edition*. Cengage Learning, 2014.

[13] M. M. Antonio Galbis, *Vector Analysis Versus Vector Calculus*. Springer, 2012.

[14] A. Solin, M. Kok, N. Wahlström, T. B. Schön, and S. Särkkä, "Modeling and interpolation of the ambient magnetic field by gaussian processes", *IEEE Transactions on Robotics*, vol. 34, no. 4, pp. 1112–1127, 2018. DOI: 10.1109/TRO.2018.2830326.

[15] N. Wahlström, "Modeling of magnetic fields and extended objects for localization applications", Ph.D. dissertation, Linköping University, 2015.

[16] *Mti user manual*, 2020. [Online]. Available: https://www.xsens.com/hubfs/Downloads/usermanual/MTi_usermanual.pdf.

[17] *Lms100-10000 product data sheet*, 2020. [Online]. Available: https://cdn.sick.com/media/pdf/1/41/841/dataSheet_LMS100-10000_1041113_en.pdf.

[18] H. Wackernagel, *Multivariate Geostatistics*. Springer, 1995.

[19] D. F. Sebastian Thrun Wolfram Burgard, *Probabilistic Robotics*. The MIT Press, 2000.

[20] E. Pedrosa, A. Pereira, and N. Lau, "Fast grid slam based on particle filter with scan matching and multithreading", pp. 194–199, 2020. DOI: 10.1109/ICARSC49921.2020.9096191.

[21] Z. Chen, "Bayesian filtering: From kalman filters to particle filters, and beyond", *Statistics*, vol. 182, Jan. 2003. DOI: 10.1080/02331880309257.